Received: 5 December 2025 | Accepted: 27 December 2025

DOI: 10.1002/hem3.70309

ARTICLE

HemaSphere eha

Wnt-dependent spatiotemporal reprogramming of bone marrow niches drives fibrosis

Bella Banjanin[1,2,^] | James Nagai[3,^] | YeVin Mun[4,^] | Stijn Fuchs[1,2] | Inge Snoeren[1,2] | Joachim Boers[1] | Mayra L. Ruiz Tejada Segura[3] | Hector Tejeda Mora[1,2] | Anna Katharina Galyga[2,5] | Adam Benabid[2,5] | Rita Sarkis[6] | Olaia Naveiras[6] | Marta Rizk[7] | Michael Wolf[7] | Rogerio B. Craveiro[7] | Fabian Peisker[8] | Ursula Stalmann[1,2] | Jessica E. Pritchard[2,5] | Hosuk Ryou[9] | Nasullah Khalid Alham[9] | Marek Weiler[10] | Fabian Kiessling[10] | Twan Lammers[10] | Anna Rita Migliaccio[11] | Kishor Kumar Sivaraj[12] | Ralf H. Adams[12] | Eric Bindels[13] | Joost Gribnau[1] | Daniel Royston[9] | Hélène F. E. Gleitz[1,2,^] | Rafael Kramann[8,^] | César Nombela-Arrieta[4,^] | Ivan G. Costa[3,^] | Rebekka K. Schneider[1,2,5,^]

Correspondence: Rebekka K. Schneider (reschneider@ukaachen.de)

Abstract

Bone marrow fibrosis is the most extensive matrix remodeling of the microenvironment and can include de novo formation of bone (osteosclerosis). Spatiotemporal information on the contribution of distinct bone marrow niche populations to this process is incomplete. We demonstrate that fibrosis-inducing hematopoietic cells cause profibrotic reprogramming of perivascular CXCL12-abundant reticular (CAR) progenitor cells, resulting in loss of their hematopoiesis-support and upregulation of osteogenic and pro-apoptotic programs. In turn, peritrabecular osteolineage cells (OLCs) are activated in an injury-specific, Wnt-dependent manner, comparable to skeletal repair. OLCs fuel bone marrow fibrosis through their expansion and skewed differentiation, resulting in osteosclerosis and expansion of Ly6a$^+$ fibroblasts. NCAM1 expression marks peritrabecular OLCs and their expansion into the central marrow is specific for fibrosis in mice and patients. Peritrabecular stromal β-catenin expression is linked to fibrosis in patients, and inhibition of Wnt signaling reduces bone marrow fibrosis and osteosclerosis, possibly being a clinically relevant therapeutic target.

[1]Department of Developmental Biology, Erasmus Medical Center, Rotterdam, The Netherlands
[2]Oncode Institute, Erasmus Medical Center, Rotterdam, The Netherlands
[3]Institute for Computational Genomics, Faculty of Medicine, RWTH Aachen University, Aachen, Germany
[4]Department of Medical Oncology and Hematology, University Hospital Zurich, Zürich, Switzerland
[5]Department of Cell and Tumor Biology, Faculty of Medicine, RWTH Aachen University, Aachen, Germany
[6]Laboratory of Regenerative Hematopoiesis, University of Lausanne, Lausanne, Switzerland
[7]Department of Orthodontics, Dental Clinic, RWTH Aachen University, Aachen, Germany
[8]Department of Medicine II (Nephrology, Rheumatology, Immunology and Hypertension), Faculty of Medicine, RWTH Aachen University, Aachen, Germany
[9]Department of Cellular Pathology, John Radcliffe Hospital, Oxford University NHS Foundation Trust, and Nuffield Division of Clinical Laboratory Sciences, Radcliffe Department of Medicine, John Radcliffe Hospital, Oxford, United Kingdom
[10]Department of Experimental Molecular Imaging, Faculty of Medicine, RWTH Aachen University, Aachen, Germany
[11]Altius Institute for Biomedical Sciences, Seattle, Washington, United States
[12]Department of Tissue Morphogenesis, Max Planck Institute for Molecular Biomedicine, Münster, Germany
[13]Department of Hematology, Erasmus MC Cancer Institute, Rotterdam, The Netherlands
^Bella Banjanin, James Nagai, YeVin Mun, Hélène F. E. Gleitz, Rafael Kramann, César Nombela-Arrieta, Ivan G. Costa, and Rebekka K. Schneider contributed equally.

INTRODUCTION

Organ fibrosis contributes to up to 45% of mortality worldwide and is characterized by extensive tissue remodeling and loss of cellular function.[1,2] The cellular origin of extracellular matrix (ECM)-producing cells in various fibrotic diseases has only recently been elucidated through the use of genetic fate tracing, time-course single-cell RNA- and ATAC-sequencing experiments,[3–5] which highlight the active tissue remodeling that co-occurs during fibrotic transformation. Bone marrow (BM) fibrosis occurs in a wide spectrum of benign and hematological malignancies, with the myeloproliferative neoplasm (MPN) primary myelofibrosis (PMF) being a prototypical example. In the context of PMF, clonal proliferation of mutated hematopoietic stem cells (HSCs) results in a sustained inflammatory milieu and the activation of BM stromal cells to produce ECM.[6–8] Alongside extensive scarring, late-stage disease features de novo formation of bone (osteosclerosis), highlighting the plasticity of broadly termed stromal cells within the BM. Yet, the pathogenesis of osteosclerosis is largely unknown. At least two anatomically distinct niches have been described in the BM: the central niche located in the inner BM and the endosteal niche, in proximity to the bone surface.[9] Functional differences between these niches have been proposed,[10] raising the possibility that cellular response to injury differs between anatomically distinct sites.

Here, we provide high-resolution single-cell and spatial analysis of the BM and specifically ask how stromal subsets change in the presence of fibrosis-inducing hematopoietic cells. For this, we utilize three distinct lineage-tracing stromal Cre-reporters. Previously, we have shown that perivascular Gli1-lineage stromal cells are expanded in kidney, lung, liver, heart, and BM fibrosis,[4,5,11] marking a therapeutically attractive cellular target. Additionally, endosteal Gli1-lineage cells were shown to be a major source of osteoblasts in the adult murine skeleton.[12] Solid organ fibrosis has traditionally been attributed to the expansion of platelet-derived growth factor receptor-β (Pdgfrb)-positive mesenchymal cells; therefore, we selected PDGFRb as a comprehensive marker for identifying these cells.[3,13] Gremlin1-positive (Grem1$^+$) cells mark a distinct osteoprogenitor population residing beneath the growth plate (GP), which we hypothesized might be involved in osteosclerosis.[14] Using the spatiotemporal resolution provided by these stromal Cre-reporters, we provide evidence that perivascular Cxcl12-abundant reticular (CAR) cells are functionally reprogrammed into fibrosis-driving cells in BM fibrosis and decrease in their frequency, leaving the endothelium exposed. This insult leads to the stepwise activation of injury-specific peritrabecular skeletal progenitor cells. Skeletal progenitor cells exit quiescence, expand, and are characterized by skewed differentiation into osteoblasts and fibroblasts (FBs), resulting in osteosclerosis and expansion of pro-inflammatory Ly6a$^+$ FBs. Mechanistically, peritrabecular progenitor cells are activated in a Wnt-dependent manner with upregulation of β-catenin. Importantly, Wnt inhibition can reduce BM fibrosis and also inhibit osteosclerosis, being a possible new therapeutic target for myelofibrosis (MF).

RESULTS

Distinct spatial macroniches can be captured by a combination of stromal Cre-reporters

We sought to map the BM stromal compartment under homeostatic, unperturbed conditions and following the induction of BM fibrosis after transplanting thrombopoietin-overexpressing (TPO-OE) hematopoietic stem and progenitor cells (HSPCs) or respective controls (empty vector, EV) into lethally irradiated mice. In order to gain a comprehensive spatial overview of the stromal populations, we utilized distinct Cre-reporter strains for lineage fate tracing: (1) Pdgfrb-CreERT2;tdTomato (Pdgfrb;tdTom), a pan-mesenchymal marker well-established in solid organ fibrosis,[3,15] (2) Gli1-CreERT2;tdTomato (Gli1;tdTom), a perivascular and endosteal stromal cell population with an established functional role in BM fibrosis,[5,12] and (3) Grem1-CreERT2;tdTomato (Grem1;tdTom), described to be an osteolineage-stromal cell population.[14]

Within bone, two major macroniches are defined as the metaphyseal region, beneath the GP, and the diaphyseal region, containing the central marrow in which the majority of hematopoietic tissue and vasculature reside (>90% of BM) (Supporting Information S1: Figure 1B).[9] The endosteal niche of the metaphysis is composed of trabecular bone and the diaphysis of compact bone.

As expected, the Pdgfrb-reporter marked abundant stromal cells after tamoxifen-induced recombination in homeostatic adult mice (Figure 1A). The central, diaphyseal marrow was filled with Pdgfrb;tdTom$^+$ interstitial, reticular-shaped cells, as well as cells surrounding arterial vessels (Figure 1A, diaphyseal panel). Within the metaphyseal region (Figure 1A), Pdgfrb;tdTom$^+$ cells were identified as both osteolineage cells and mature osteocytes embedded in the bone matrix, highlighting their active contribution to osteogenesis.

Gli1;tdTom$^+$ cells were residing in the peritrabecular region of the metaphysis (Figure 1A), particularly present in the GP and within the compact bone (diaphysis), in line with their known role in postnatal bone formation.[12] Gli1;tdTom$^+$ cells also had a very specific perivascular position in the diaphysis, wrapping around the central artery, a location previously not appreciated at this resolution. Grem1;tdTom$^+$ cells were the least abundant cell population representing singular chondrocyte columns in the GP, and a few reticular-shaped cells growing out from the GP (Figure 1A), confirming previous reports.[14] Importantly, Grem1-tdTom$^+$ cells were not detected in the central marrow of mice (Figure 1A, femur overview). The distinct location of these stromal subsets throughout the metaphysis and diaphysis suggested different functions of the targeted stromal cells.

To obtain high-resolution data of these lineage-traced stromal cells in homeostasis and to compare the cellular and transcriptional changes occurring during extensive remodeling of the stroma in BM fibrosis, we performed single-cell RNA sequencing (scRNAseq) on tdTomato$^+$ cells isolated from the three Cre-reporters (Pdgfrb;tdTom, Gli1;tdTom, and Grem1;tdTom) in homeostasis, BM fibrosis (disease), and respective control conditions. We sort-purified Lin^{neg}CD45^{neg}tdTom$^+$ cells from lineage-depleted BM and digested bone chip (BC) fractions (gating Supporting Information S1: Figure 1A). An initial clustering after batch correction and integration identified 15 clusters, which displayed distinct levels of tdTomato expression (Supporting Information S1: Figure 1B,C). We excluded cell clusters with low numbers of cells characterized as non-stromal cells (hematopoietic, neuronal, and skeletal muscle cells) from further analysis, resulting in a single-cell experiment with 29,742 cells and a mean genes per cell of 2337. A high granularity re-clustering of the data recovered 30 clusters, which are associated with six major cell populations (Figure 1B): CAR cells (CAR1-7, IFN_CAR, and MusCAR), FBs (FB1-8 and IFN_FB), osteolineage cells (OLC1-3 and osteoblasts; OB), chondrocytes (chondro and pre-chondrocytes), stromal cells (including smooth muscle cells), and endothelial cells (Endo1; Endo2), including associated pericytes sub-populations. These are supported by the expression of *Cxcl12* (CAR), *Bglap* (OB), *Dcn* (FB), and *Pecam1* (Endo + pericytes) (Figure 1C; Supporting Information S1: Figure 1D).

Prompted by the specific spatial location of the Cre-reporters in imaging, we derived expression signatures from a recently published

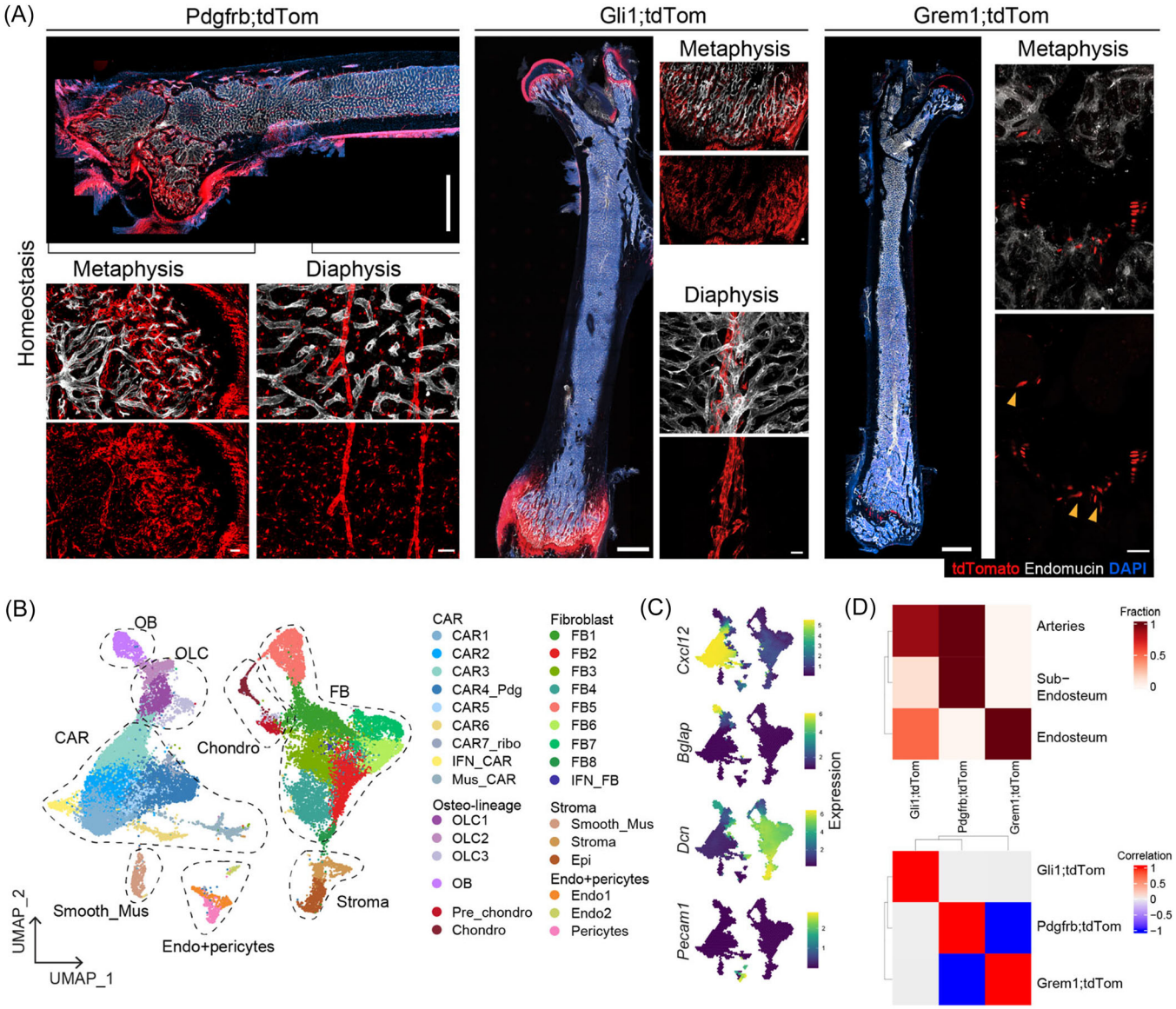

FIGURE 1 **The combination of stromal Cre-reporters provides high granularity of the bone marrow (BM) stromal niche. (A)** Whole-mount imaging of homeostatic ("homeo") femurs in unperturbed Pdgfr;tdTomato; Gli1;tdTomato, and Gremlin1;tdTomato adult mice 21 days after tamoxifen injections. 4′,6-diamidino-2-phenylindole (DAPI) as nuclear staining (blue) and endomucin (white) to depict vasculature. Yellow arrowheads show sparse Grem;tdTom$^+$ cells emerging from the growth plate. Whole femur overviews scale bar = 1000 µm, zoomed-in panels scale bar = 50 µm. **(B)** UMAP representation of 29,742 cells based on the integration of 11 individual single-cell RNA sequencing (scRNAseq) libraries (n = 40 mice). Major cell type annotations are shown. CAR, CXCL12-abundant reticular cells; chondro, chondrocytes; endo, endothelial; epi, epithelial; FB, fibroblasts. **(C)** Density of expression values after magic imputation for marker genes of major cell types. **(D)** Deconvolution analysis of scRNAseq data from (B) per distinct Cre-reporter to microdissected bulk-RNA sequencing of BM region signatures defined by Baccin et al.[16] Top panel shows the proportion of cells within whole Cre-reporter assigned to each region, and the bottom panel shows the correlations between the proportion of Cre-reporters.

bulk-RNAseq dataset of laser-microdissected regions of homeostatic BM that define the endosteum-, sub-endosteum (marrow close but not adjacent to the endosteum), sinusoidal, and arterial areas[16] to predict the spatial localization of the stromal cell clusters. The bulk-RNAseq-derived sinusoidal niche signature contained mainly hematopoietic genes and was not retrievable in our deconvolution analysis, as our data are enriched in stromal cells. Strikingly, and in line with the imaging, the Gli1;tdTom dataset was highly enriched in the arterial and endosteal signatures, the Pdgfrb;tdTom dataset confirmed the observation of widespread representation of Pdgfrb-lineage cells within the BM, and the Grem1;tdTom dataset was limited to the endosteal signature (Figure 1D). We thus recovered the "location stamp" of the tdTom$^+$ cells within the transcriptome of single cells.

Fibroblasts expand in BM fibrosis, while CAR cells are depleted after reprogramming and upregulation of collagen

To evaluate the cellular changes occurring during BM fibrosis, tamoxifen-mediated recombination of stromal Cre-reporters was

induced in adult mice. In MPN, the thrombopoietin receptor MPL is activated by the three driver mutations of MPNs (JAK2, CALR, or MPL mutations) or can be directly activated by its ligand thrombopoietin (TPO). MPL activation is indispensable for MPN development regardless of the MPN driver mutation. The overexpression of thrombopoietin (TPO-OE) was used as a well-established model of MF and osteosclerosis.[17] c-Kit$^+$ HSPCs were lentivirally transduced with the TPO-OE plasmid or the respective EV control and transplanted into the lethally irradiated stromal Cre-reporter mice (Figure 2A). TPO-OE transplanted mice developed a robust phenotype of myeloproliferation reflected by high platelet and white blood cell counts, and a drop in hemoglobin (Hgb) and BM cellularity due to reticulin fibrosis, which was accompanied by splenomegaly with extramedullary hematopoiesis (Supporting Information S1: Figure 2A–D).

ScRNAseq of tdTom$^+$ cells from all Cre-reporters demonstrated that CAR cells were the most abundant tdTom$^+$ stromal cell type in the control condition (EV), in line with the literature and their central role in hematopoiesis-support (Figure 2B,C). In fibrosis (TPO-OE), OLC-, FB-, and chondrocyte-like cells were enriched within the sorted tdTom$^+$ fractions, while all CAR cell populations were less represented. This is a fibrosis-specific response, as after irradiation and transplant (EV condition), we saw an increase of CAR and endothelial cells compared to the unperturbed niche (homeo) (Supporting Information S1: Figure 2E). We were intrigued by the expansion of FBs in BM fibrosis, as FB subsets were described as central players in solid organ fibrosis.[3,19] In the BM, FBs have been rather poorly defined, particularly in response to hematological malignancy.

We thus explored our data for characterizing markers to discriminate FBs from other stromal cells by applying sc2marker.[20] *Ly6a* was ranked as the top marker for FB identification (Figure 2D). *Ly6a* encodes for Sca-1 glycoprotein, classically used to enrich HSCs from adult murine BM. Importantly, we did not observe an increase in *Ly6a* expression in the fibrotic marrow in non-FB populations and endothelial cells, thus making it an attractive marker to study the FB fate (Supporting Information S1: Figure 2F). To validate that Ly6a$^+$ FBs expand in BM fibrosis, we used a Ly6a-GFP transgenic mouse strain[21] to label Ly6a$^+$ cells upon fibrosis induction (Figure 2E). To avoid hematopoietic-derived Ly6aGFP signal, we performed a BM transplantation into Ly6a-GFP recipients with WT donor cells that were transduced with EV- or TPO-OE-BFP constructs (Figure 2E). The TPO-OE mice developed a typical myeloproliferative phenotype (Supporting Information S1: Figure 2G–I). To account for endothelial cells being marked by *Ly6a* expression, we stained sections from the transplanted mice with the vascular marker endomucin (Emnc). In control conditions, Ly6a-GFP$^+$Emnc$^+$ cells were mostly found in perivascular localization, highlighting endothelial cells and pericytes (Figure 2F). In fibrotic BM, Ly6a-GFP$^+$Emnc$^-$ cells were massively expanded in the central marrow, partially in association with the vasculature but also in clusters of cells without direct vascular contact (Figure 2F).

We next asked how the expression profiles changed after induction of BM fibrosis. CAR cells had the highest number of differentially expressed genes (DEGs), followed by osteolineage cells (OLC1) and also a subcluster of endothelial cells (Endo-1; Figure 2G). In contrast, FBs, as the most expanded cell population, only showed minor transcriptional changes. CAR1 cells mainly upregulated collagen and ECM signature genes (*Col1a1*, *Col3a1*), matrix remodeling genes (matrix metalloproteinases *Mmp2*, *Mmp9*), and increased bone metabolism (*Apod*) (Figure 2H).[22] In line with previous findings,[8] CAR1 cells decreased their hematopoiesis-supporting capacity (*Cxcl12*, *Lpl*, and *Kitl*) (Figure 2H). The most significant upregulation of profibrotic TGFβ signaling, as the master switch of fibrosis, occurred in CAR cell subsets, alongside an enrichment of epithelial-mesenchymal transition signatures (Figure 2I). BM-resident FBs (here exemplary FB4 as population with highest DE genes) mainly gained an inflammatory signature, with upregulation of chemokines (*Ccl2*, *Ccl7*), components of the complement system (*C3*) (Figure 2H), and NF-kB-mediated induction of inflammation (Figure 2I). While CAR cells also gained a pro-inflammatory and increased apoptotic signature in the fibrosis setting, FBs in fibrosis were mainly characterized by a pro-inflammatory state known to play a role in the profibrotic signaling and remodeling of the microenvironment.

Assessing the aggregate expression of collagen proteins[23] per cluster (Figure 2J), almost all CAR cell subsets showed an upregulation of collagen in exposure to TPO-OE hematopoietic cells. Interestingly, the transcriptionally most active subsets of osteolineage cells (OLC1) and endothelial cells (Endo-1) also upregulated collagen expression. It is important to mention here that FBs at baseline already have high expression of collagens and might, by expanding, also contribute to the fibrotic transformation of the BM (Figure 2K).

Distinct stromal phenotype switch in metaphyseal and diaphyseal localization during fibrotic transformation

As the stromal Cre-reporters occupy distinct anatomical regions of the BM (compare Figure 1), we aimed to gain more spatial information on fibrosis formation by performing BM 3D confocal microscopy (Figure 3; Supporting Information S1: Figure 3).

tdTom$^+$ cells from all Cre-reporters were activated by the presence of TPO-OE cells (Figure 3; Supporting Information S1: Figure 3), but in distinct regions of the BM. While Pdgfrb;tdTom$^+$ cells expanded in the diaphyseal region in BM fibrosis, the largest expansion was seen in the metaphysis, surrounding trabecular bone (Figure 3A,B). Within the metaphysis of fibrotic marrows, we observed signs of osteosclerosis, highlighted by Pdgfrb;tdTom$^+$ cells expressing podoplanin, and their osteolineage-like morphology (Supporting Information S1: Figure 3A). The Grem1;tdTom reporter was specifically detected in the metaphysis, marking chondrocyte columns in the GP, but Grem1;tdTom1$^+$ cells showed only subtle changes after exposure to TPO-OE hematopoietic cells. Sparse, reticular-shaped Grem1;tdTom$^+$ cells started to emerge from the GP (Supporting Information S1: Figure 3B, arrowheads).

Gli1;tdTom$^+$ stromal cells showed two distinct activation patterns upon fibrotic activation: increased frequency and expansion in the endosteal region of the metaphysis, and detachment from vasculature in the diaphysis (Figure 3C). In the diaphysis, Gli1;tdTom$^+$ stromal cells increased in size, and gained an activated, myofibroblast-like morphology with long cellular extensions compared to cells in the control setting (Figure 3D,E). In these areas, endothelial cells also appeared activated, most likely due to the detachment of tdTom$^+$ stromal cells from the vascular wall, leaving endothelial cells unprotected and exposed to the cytokine- and growth factor-rich environment caused by the fibrosis-inducing hematopoietic cells. The vascular bed in fibrotic marrow generally became more disorganized (compared Figure 3A–E; Supporting Information S1: Figure 3B). This is in line with transcriptional changes found in the Endo-1 cluster detected in the scRNAseq (Supporting Information S1: Figure 3C). This cluster showed upregulation and expression of apelin, a marker for H-vessels, only in fibrosis, and an increase in endothelial-to-mesenchymal transition (endoMT; Supporting Information S1: Figure 3D).[24]

Thus, the most distinct hotspot of tdTom$^+$ stromal cell expansion in BM fibrosis in all Cre-reporters was within the metaphyseal region (Figure 3A–C; Supporting Information S1: Figure 3A, B, and E). Spatiotemporal resolution combining a time-course experiment with confocal imaging demonstrated the activation of Gli1;tdTom$^+$ stromal cells in the metaphysis in a stepwise manner (Figure 3F). In the early phase (low-grade fibrosis), spindle-shaped cells emerged from the trabecular bone of

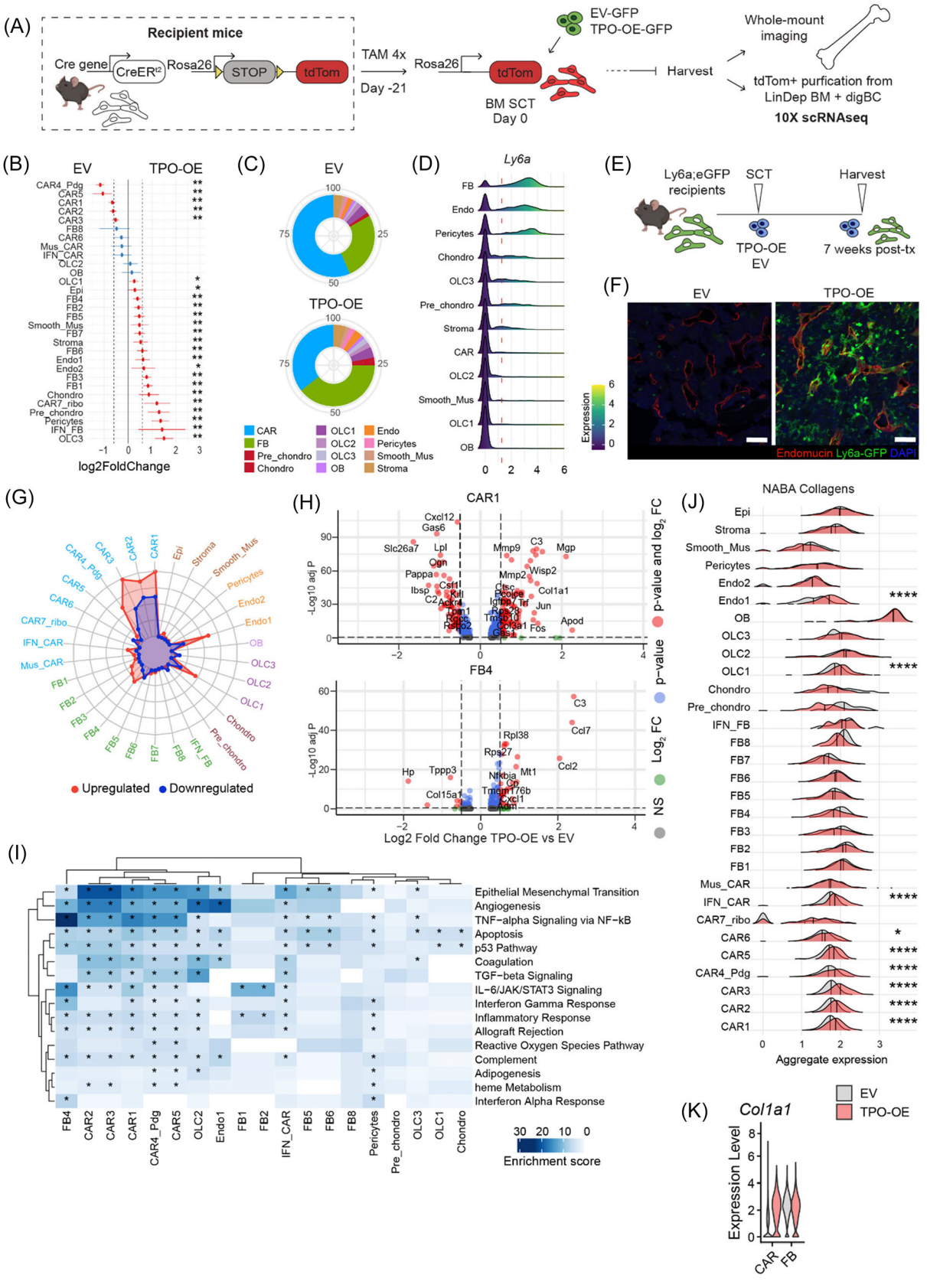

FIGURE 2 (See caption on next page).

FIGURE 2 **CXCL12-abundant reticular (CAR) cells acquire a profibrotic phenotype but are reduced in frequency while fibroblasts expand in bone marrow fibrosis. (A)** Experimental design: bigenic CreER;tdTomato mice were injected with tamoxifen (TAM), lethally irradiated at 21 days after the last tamoxifen dose, and intravenously received c-Kit-enriched hematopoietic stem cells (HSCs) from wild-type (WT) littermates expressing either thrombopoietin complementary DNA (cDNA) (TPO-OE) or control (empty vector; EV) cDNA (both lentiviral SFFV-iGFP vector backbone). BM SCT, bone marrow stem cell transplant. **(B)** Proportion test of cells per cluster (TPO-OE vs. EV) obtained using scProportionTest. Relative differences in cell proportion per cluster, red colored dots show significant fold change (false discovery rate, FDR < 0.05 and absolute fold change > 0.58) with error bars showing confidence intervals for the magnitude difference (permutation test, $n = 1000$). Blue dots: not significant; red dots: significant changes. **(C)** Contribution of individual clusters to all recovered cells per Cre-driver, comparing the control (EV) to the fibrosis (TPO-OE) condition. **(D)** Ridge plot of *Ly6a* expression per cluster. Clusters are ordered according to mean *Ly6a* expression values. **(E)** Ly6a;eGFP mice were lethally irradiated and intravenously received c-Kit-enriched HSCs from WT littermates expressing either thrombopoietin cDNA (TPO-OE; $n = 5$, three males) or control cDNA (EV, $n = 5$; both lentiviral SFFV-iblue fluorescent protein [BFP] vector backbone), scale bar = 100 µm. **(F)** Representative images of TPO-OE BM of Ly6a;GFP mouse, Endomucin in red, 4′,6-diamidino-2-phenylindole (DAPI) nuclear stain in blue, scale bar = 100 µm. **(G)** Radar plot of the number of differentially expressed genes per cluster (TPO vs. EV). **(H)** Representative volcano plots (TPO-OE vs. EV) of differentially expressed genes in CAR1 and FB4. **(I)** Heatmap of enrichment scores using EnrichR of the upregulated differentially expressed genes (TPO vs. EV), genes with P-value < 0.05 were considered. Significance of the enrichment test was obtained using Fisher's exact test implemented by EnrichR. **(J)** Aggregate expression of NABA collagens for all clusters (gene sets from Ref. 18). One-sided Wilcox test compared the expression of EV and TPO. **(K)** Collagen1a1 (*Col1a1*) expression in CAR cells and fibroblasts (FB) in TPO-OE versus EV control. Statistical significance is indicated by *P < 0.05, **P < 0.01, ***P < 0.001, and ****P < 0.0001.

the metaphysis and increased over time into the central marrow. In progressed fibrosis (late), dense nests of Gli1;tdTom$^+$ cells were found broadly beneath the GP with activated morphology. To assess the activation of Gli1;tdTom$^+$ cells from metaphysis to diaphysis, we quantified the progression of tdTom-signal from the GP to central marrow (Figure 3G). Here, we found a stepwise increase in the tdTom signal in fibrotic marrow compared to EV controls, with increases of tdTom signal present even in early-stage disease. We included an additional model of BM fibrosis by transplanting c-Kit$^+$ cells transduced with the MPLW151L (MPL) as a common MPN and MF-driver mutation[6] into Gli1;tdTom recipient mice. It is important to note that the retroviral MPL murine model is characterized by strong myeloproliferation but less severe fibrosis compared to the TPO-OE model (compare fibrosis grades Figure 3H; Supporting Information S1: Figure 3F).[6] We observed a notable increase in Gli1;tdTom$^+$ mobilization in the more fibrotic TPO-OE marrows, unlike in MPL-transplanted marrows (Supporting Information S1: Figure 3G), indicating that advanced fibrosis is associated with enhanced Gli1;tdTom$^+$ expansion into the BM. We overlaid a reticulin staining on the imaged tdTomato signal after demounting of slides in the Pdgfrb-reporter (Supporting Information S1: Figure 3E). Interestingly, the tdTom$^+$ hotspots completely aligned with the hotspots of reticulin deposition in the metaphyseal region, while reticulin deposition in the diaphyseal region of the same bone was rather minor (Supporting Information S1: Figure 3E). In line with this, we quantified reticulin fibrosis in the metaphysis and diaphysis of the same bone, and found significantly higher fibrosis in the metaphyseal region in both the TPO-OE (Figure 3H) and MPL models (Figure 3H; Supporting Information S1: Figure 3F). This data suggests that an injury-specific stromal population resides within the metaphysis, which is essential for the fibrotic transformation.

OLC3 represent stromal progenitor cells and reside in the metaphysis of the bone marrow

We hypothesized that the metaphyseal (trabecular bone) and diaphyseal (compact bone) regions contain stromal cells with distinct functions and differentiation potentials, in line with reports on skeletal repair.[25] Specifically, we asked if the peritrabecular region is a reservoir for stromal and fibrosis-driving cells, which react to injury/inflammatory stimuli.

We thus sought to (1) establish a stromal cell hierarchy and (2) assess the lineage trajectories and cell fates of these populations. We applied PHATE visualization reduction of the data, focusing on disease-relevant cell types with significant numerical or transcriptional changes: CAR cells, FBs, OLCs, chondrocytes, and terminally differentiated osteoblasts (Figure 4A, compare to Figure 2). In this projection, OLC3 cells were positioned as a central hub connecting CAR cells, pre-chondro- and chondrocytes, and FBs (Figure 4A). In a different PHATE projection, OLC3 were positioned at the apex of the differentiation hierarchy, demonstrating connections to the CAR4_Pdg cluster, the pre-chondro and FB clusters, as well as the mature OBs and chondrocytes (Supporting Information S1: Figure 4A).

To achieve an unbiased view of the progenitor and expansion potential of the stromal clusters, we explored both the coefficient of variance score of cells (as a surrogate marker for stemness or specialization) and their cell cycle status. In brief, cells with a higher coefficient of variance have highly specialized expression of genes, termed "SPEC," supporting a differentiated state. In contrast, cells with a lower coefficient of variance, termed "MONO" or monotonous, do not display any specific expression pattern as typically seen in progenitor-like cells. The application of these scores suggested that CAR4_Pdg is a stem and progenitor cell population (low SPEC and high MONO), and the osteoblast- and chondrocyte clusters scored highly as differentiated cells (high SPEC and low MONO) (Supporting Information S1: Figure 4B). Next, we concentrated on the cell cycle state of cells. We observed a significant increase in the G2 cell cycle stage in OLC3 and pre-chondro populations in TPO-OE versus EV, and a reduction of these populations in G1 cell cycle stages (Figure 4B; Supporting Information S1: Figure 4C). OLC3 cell populations also displayed an intermediate stemness (MONO) and a low specialization (SPEC) score. This indicates a progenitor role of the OLC3 cluster, while its proliferation in fibrosis suggests the activation in response to tissue injury.

We used this information to estimate trajectories and pseudotime using ArchR and PHATE (Figure 4C). In PHATE visualization, three distinct trajectories appeared: (1) an "osteo-primed trajectory" through CAR1/3/5, OLC1/2/3 toward mature OBs, (2) an "chondro-primed" trajectory via OLC3 toward chondrocytes, and (3) a "FB primed" trajectory through OLC3 toward FBs. We next ran pseudotime analysis along the trajectories. Cells showed an increase in specialization (decrease in stemness) scores in pseudotime (Supporting Information S1: Figure 4D). The osteo-, chondro-, and FB- trajectories were increased in BM fibrosis (TPO-OE). The increased differentiation into FBs indicates that their abundance in the BM in fibrosis can be explained by activation of progenitor cells.

To explore the spatial relevance of fibrosis deposition in the BM, we mapped scRNAseq clusters to their spatial localization in the BM, using a published dataset defining regional specifications of metaphyseal and diaphyseal BM stromal cells.[25] Label transfer analysis showed that most CAR clusters, including CAR4-Pdg, were associated with a diaphyseal signature, while some had a mixed location, likely representing a transition zone (Figure 4D,E). Metaphyseal signatures

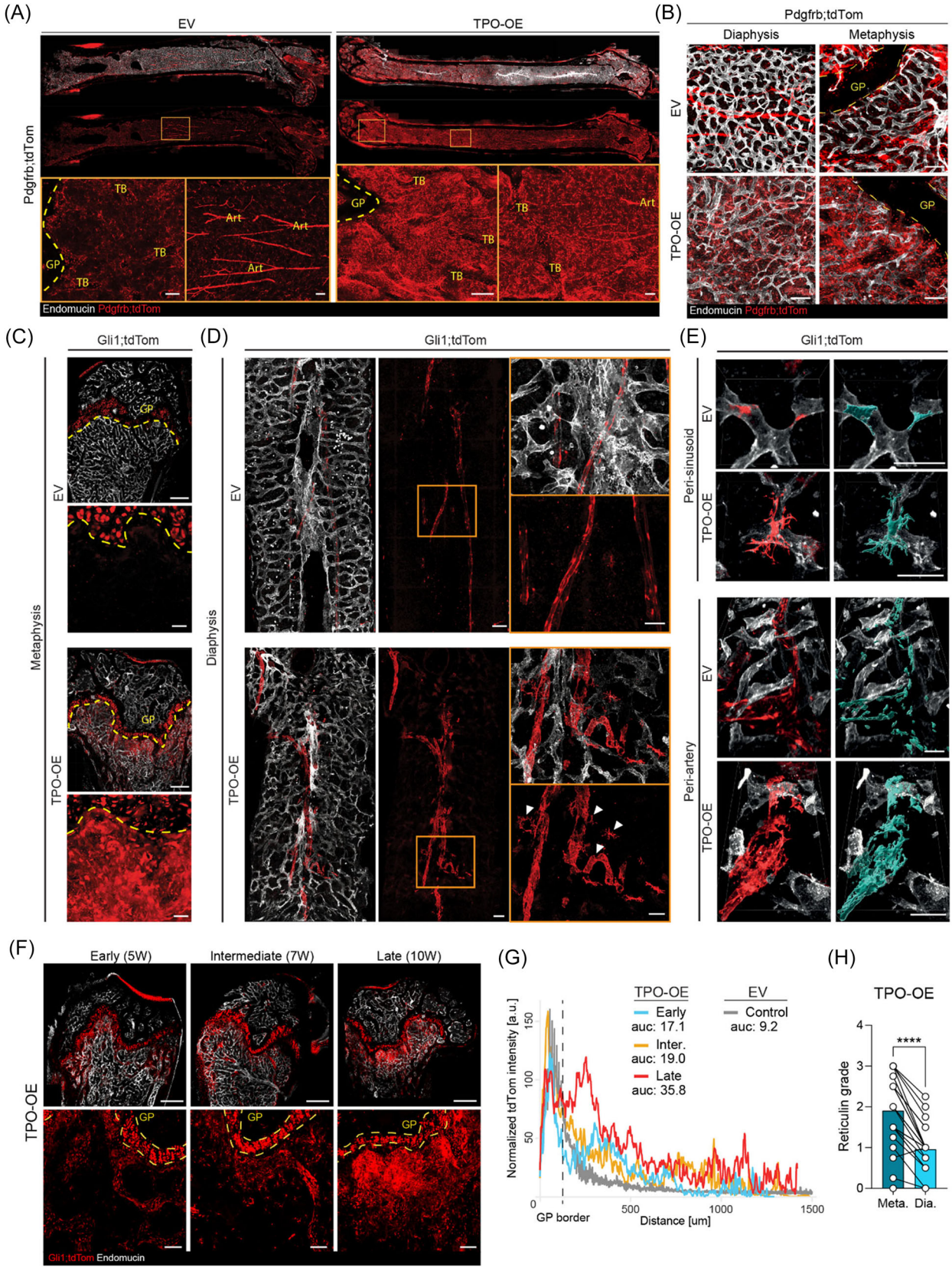

FIGURE 3 (See caption on next page).

FIGURE 3 **Distinct phenotype switch in thrombopoietin overexpression (TPO-OE) induced bone marrow fibrosis in the diaphyseal and metaphyseal localization**. **(A)** Representative whole-mount confocal images of Pdgfrb;tdTom femurs and zoom-in at indicated regions of the bone, EV = empty vector (control) and TPO-OE (fibrosis). Art, arteries; TB, trabecular bone; dotted line demarcates the growth plate (GP). Scale bar = 100 μm. **(B)** Representative whole-mount confocal images of Pdgfrb;tdTom femurs at indicated regions of the bone, EV (control) and TPO-OE (fibrosis). Dotted line demarcates the GP, scale bar = 100 μm. **(C)** Overview of whole bone of control (EV) and fibrotic Gli1;tdTom femurs, representative whole-mount confocal images. Dotted line demarcates the GP. Scale bars = 300 μm. Lower panel is a zoom-in of the metaphyseal region in EV and TPO-OE, respectively, scale bars = 20 μm. **(D)** Diaphyseal region of Gli1;tdTom bones, with Gli1-lineage cells wrapping around the central artery in control (EV) and fibrosis (TPO-OE) shown with and without endomucin co-staining. Boxes in the middle panel highlight the zoom-ins in the right panel. Note the detaching, large stromal cells leaving the arterial walls in the fibrotic setting, highlighted by the white arrow heads. Scale bars, middle panel = 100 μm; scale bars, zoomed-in panel = 50 μm. **(E)** Morphological switch of Gli1;tdTom$^+$ cells in perisinusoidal and periarterial location in fibrosis (TPO-OE) compared to control (EV). Representative whole-mount confocal images of single cells are shown. Mask of Gli1;tdTom channel shown in blue. Scale bar = 50 μm. **(F)** Whole-mount confocal visualization of time-course Gli1;tdTom$^+$ cell expansion after transplant with TPO-OE c-Kit-enriched cells. Early = 5 W post-Tx, intermediate = 7 W post-Tx, and late = 10 W post-Tx. Scale bar, top panel: 500 μm, bottom panel: 50 μm. Dotted line demarcates the GP. **(G)** Quantification of Gli1;tdTom$^+$ cell expansion/movement away from the GP border from panel (F). Inter., intermediate; auc, area under the curve from the GP border, measured per line profile shown. **(H)** Reticulin grading of fibrosis according to World Health Organization (WHO) criteria in the metaphysis (meta) compared to the diaphysis (Dia). Statistical significance is indicated by *P < 0.05, **P < 0.01, ***P < 0.001, and ****P < 0.0001.

were enriched in chondrocytes, FBs, and OLCs—the cell types predominantly found in TPO-OE BM (Figure 2B). Comparing TPO-OE to EV metaphyseal and diaphyseal signatures, we observed a loss of diaphyseal-location signature in CAR clusters, suggesting perivascular detachment and fibrotic reprogramming (Figure 3). Osteo-primed CAR3 and OLC3 showed an increase in metaphyseal signatures, indicating peritrabecular expansion, while the metaphyseal signature of FBs and OLC1 decreased in TPO-OE. Ly6a$^+$-FBs, typically absent in the diaphysis at steady state, were abundant in fibrosis (Figure 2F).

We thus wondered how the different Cre-drivers contribute to OLC in control (EV) and fibrosis (TPO-OE). While under control conditions, Pdgfrb;tdTom$^+$ cells mostly contribute to OLCs, these subsets are mostly derived from Gli1;tdTom$^+$ cells in fibrosis, confirming the fibrosis-specific activation of Gli1$^+$ cells (Figure 4F).

To functionally validate the stem and progenitor potential of cells in the metaphyseal region, we sort-purified tdTom$^+$ cells from the metaphyseal and diaphyseal regions of long bones of unperturbed, homeostatic mice (Figure 4G). By applying the Pdgfrb;tdTom reporter for broad stromal lineage marking, we saw comparable tdTom$^+$ fluorescent signal strengths between metaphyseal and diaphyseal tdTom$^+$ cells, with similar frequencies of tdTom$^+$ cells between the macroniches (Supporting Information S1: Figure 4E). Remarkably, only tdTom$^+$ cells isolated from the metaphysis regions of long bones harbored colony-forming potential, and diaphyseal tdTom$^+$ cells from the same bones did not give rise to FB colonies in vitro (Figure 4H). Gli1;tdTom cells were mainly located in the metaphyseal region in homeostatic mice (Supporting Information S1: Figure 4F). Sorted Gli1;tdTom$^+$ cells from the metaphyseal region contained a high number of fibroblastic colony-forming units (CFU-Fs), supporting their progenitor-cell state (Figure 4I).

To validate that Pdgfrb;tdTom$^+$ and Gli1;tdTom$^+$ cells can mark long-lived mesenchymal progenitor cells, we induced recombination in adult mice and harvested bones more than one year after the last tamoxifen injection (Supporting Information S1: Figure 4G). Pdgfrb;tdTom$^+$ cells were distributed across all compartments of the bone (metaphysis, diaphysis), whereas Gli1;tdTom$^+$ cells were mainly positioned in the metaphysis and were less present in the diaphysis. Comparing the Pdgfrb;tdTom and Gli1;tdTom reporters in homeostatic conditions revealed that the Pdgfrb-reporter is enriched for CAR4_Pdg cells (stromal stem cell). In contrast, Gli1$^+$ cells are mainly enriched for the OLC3 population (Supporting Information S1: Figure 4H). We thus propose that PdgfrbCre;ERT2 labels a perivascular stromal stem cell (CAR4_Pdg) that replenishes the BM stromal population under physiological conditions, and Gli1Cre;ERT2 labels a peritrabecular mesenchymal progenitor cell population (OLC3) that is activated in an injury-specific manner from their peritrabecular localization.

CAR and OLCs are skewed in their differentiation in BM fibrosis

We hypothesized that the fate of the peritrabecular OLC3 and perivascular CAR4_Pdg stem and progenitor cells is skewed in the presence of fibrosis-inducing hematopoietic cells and an inflammatory environment. We indeed observed distinct histomorphological changes in fibrotic BM compared to non-fibrotic controls. After irradiation, control BM (EV) typically depicts adipocytes in the metaphyseal region (Figure 5A). In contrast, fibrotic marrows were almost devoid of adipocytes (Figure 5A). This change was quantifiable using MarrowQuant.[26] Non-hematopoietic and non-vascular cellular components were expanded in fibrotic (TPO-OE) marrows, while the adipocyte area and number of adipocytes decreased (Figure 5B,C).

The pattern of decreased adipocytes in fibrosis was confirmed in other murine models of myeloproliferation associated with MF: JAK2V617F- and MPLW515L-mutated disease (Supporting Information S1: Figure 5A). Importantly, the decrease in adipogenesis was confirmed in BM biopsies of MPN patients and specific to MPN with fibrosis, not MPN per se (Figure 5D,E), indicative of skewed differentiation of mesenchymal progenitor cells in fibrosis.

Given this apparent change in stromal differentiation in the context of BM fibrosis, we explored the expression of adipocyte (adipo), osteoblast (osteo),[25] and chondrocyte (chondro)[27] specific genes within our scRNAseq dataset (Figure 5F; Supporting Information S1: Figure 5B, gene sets in Supporting Information S3: Table 2). The average expression of these genes per cluster grouped the homeostatic dataset into more adipo-primed (CAR cells) and osteo-primed cell clusters (OLCs and OBs) (Supporting Information S1: Figure 5C). CAR3 were, however, more osteo-primed as indicated by relatively higher expression of *Spp1*, *Alpl*, *Sp7*, and *Wif1* compared to other CAR populations. OLC1 is a predominantly osteo-primed population, but still expresses *Foxc1*, *Gas6*, and *Apoe*. In fibrosis, a distinct skewing in the differentiation was observed: CAR cells, OLC1, and OLC3 significantly decreased their expression of adipo-genes, while specifically CAR cells increased the expression of osteo-genes (Figure 5F). The skewed differentiation was also obvious in chondro-linked genes in the fibrotic setting, specifically in the CAR populations and OLC3, potentially hinting at calcification occurring in these cells upon fibrotic transformation (Supporting Information S1: Figure 5B). The increase of osteo-associated genes in fibrotic marrows was also

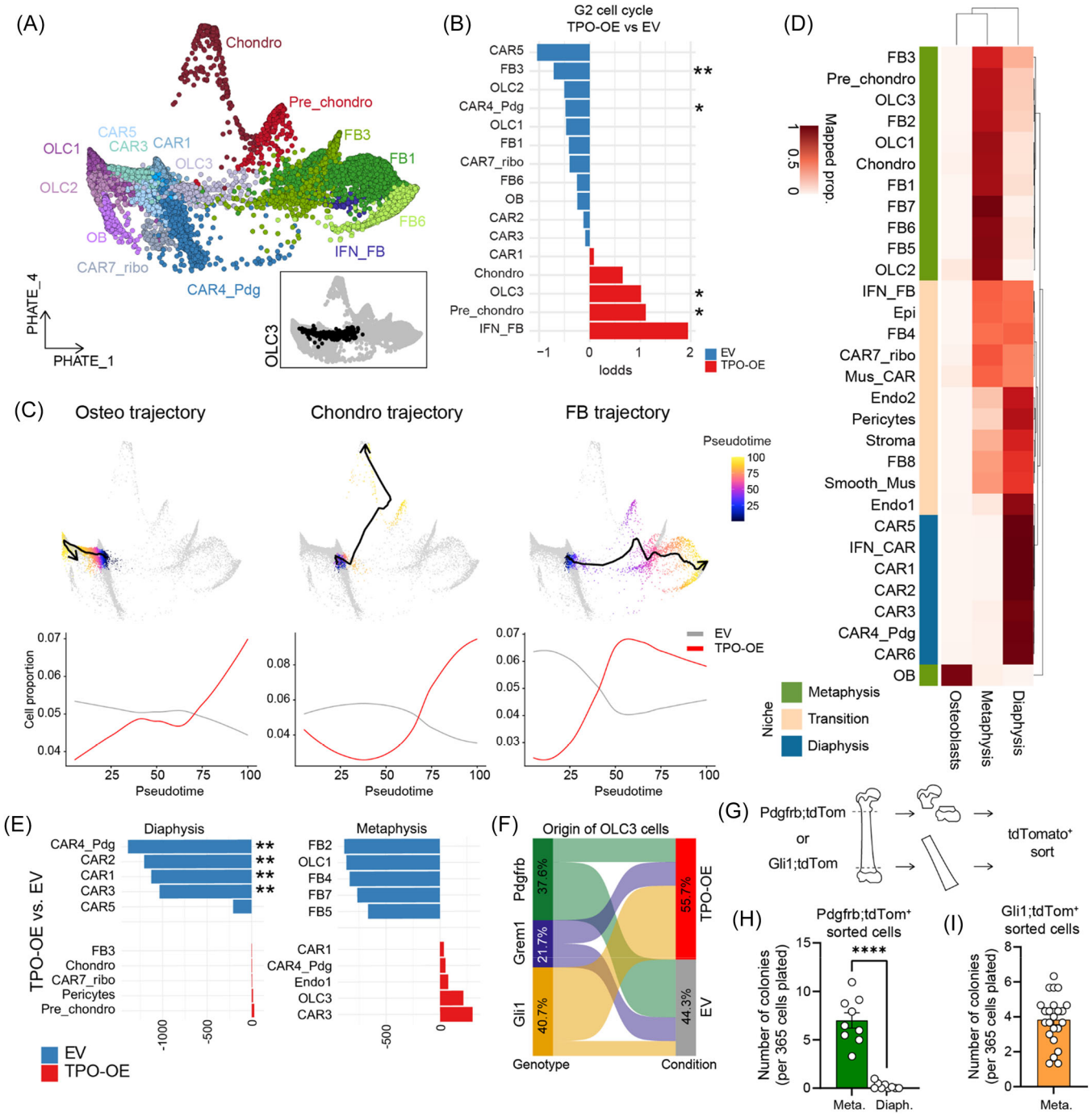

FIGURE 4 **Osteolineage cells (OLCs), as progenitor cells of the bone marrow, are enriched in the metaphysis in bone marrow fibrosis.** **(A)** PHATE dimension reduction of CXCL12-abundant reticular (CAR), OLC, and fibroblast (FB) cells indicates potential cell differentiation trajectories. Inset in the lower right corner showing PHATE visualization with the OLC3 cluster highlighted in black. **(B)** Cell cycle G2 proportion analysis in stromal cell clusters, comparing thrombopoietin overexpression (TPO-OE) versus empty vector (EV) control. Statistical comparison was done using Fisher's exact test. **(C)** Trajectory analysis of CAR cells/OLCs toward osteo, chondro, and FB cells (top). Proportion of cells in EV or TPO conditions along pseudotime (bottom) per experimental condition. **(D)** Proportion of cells assigned to "diaphysis," "metaphysis," and "osteoblast" reference cell dataset (source Srivaja et al. dataset). **(E)** Difference in the absolute proportion of cell clusters associated with diaphysis and metaphysis in TPO versus EV conditions. Asterisks represent cells with differences larger than two standard deviations around the mean. **(F)** Sankey plot showing the origin of OLC3 cells by genotype and condition. **(G)** Experimental setup on the isolation of cells from the metaphyseal (peritrabecular) compared to the diaphyseal region of homeostatic Cre-reporter lineage-traced bones. **(H)** Quantification of fibroblastic colony-forming units (CFU-Fs) of sort-purified Pdgfrb;tdTom$^+$ cells ($n = 3$ biological replicates, three technical replicates, data are presented as mean ± SEM, two-tailed unpaired t-test). Meta., metaphyseal region; Diaph., diaphyseal region. **(I)** Quantification of CFU-Fs of sort-purified Gli1;tdTomato$^+$ cells ($n = 4$ biological replicates, 5–6 technical replicates, data are presented as mean ± SEM). Meta., metaphyseal region; Diaph., diaphyseal region. Statistical significance is indicated by *P < 0.05, **P < 0.01, ***P < 0.001, and ****P < 0.0001.

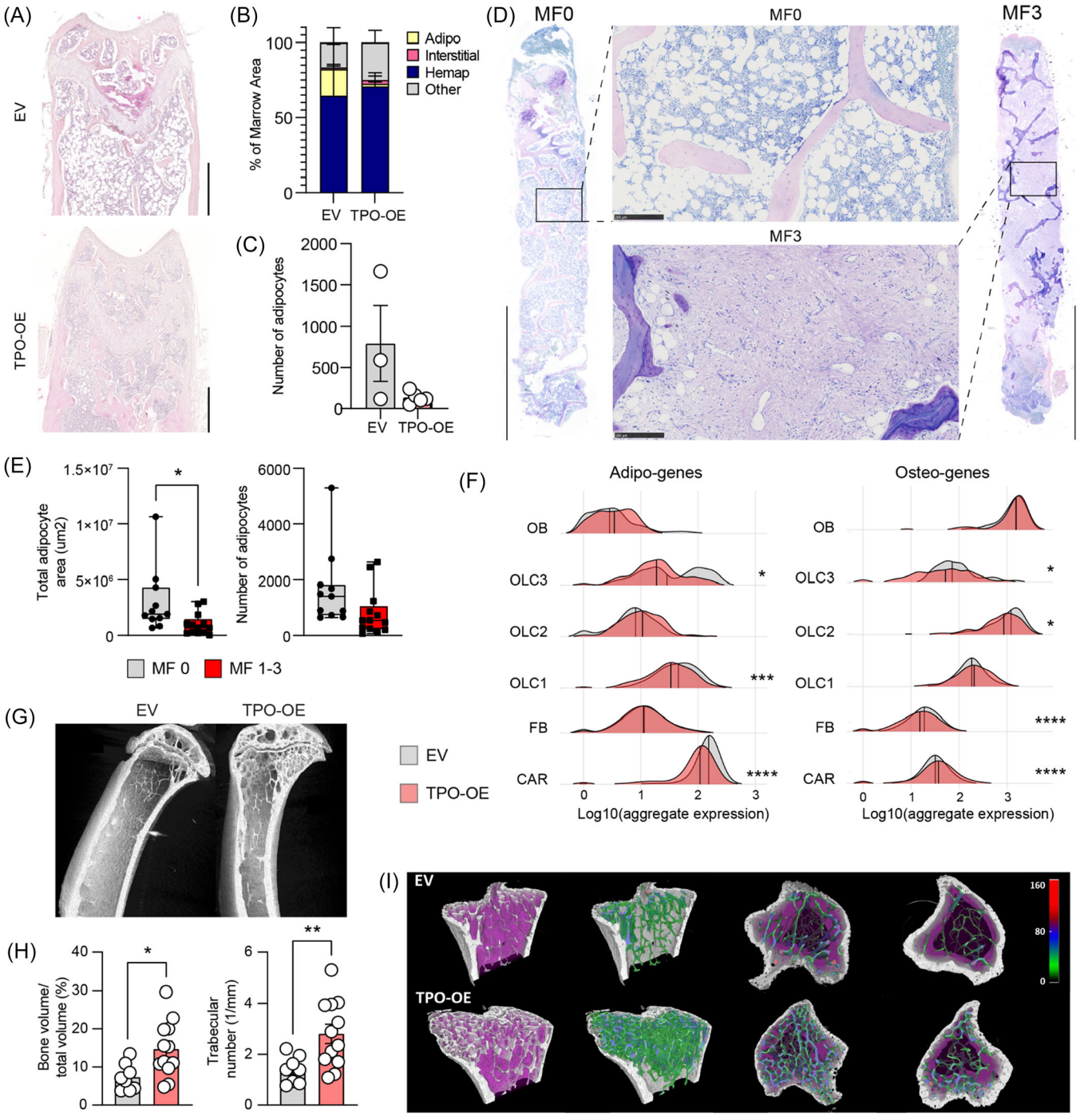

FIGURE 5 **Stromal stem and progenitor cells are skewed in their differentiation in bone marrow fibrosis**. **(A)** Representative images of hematoxylin and eosin (H&E) staining of wild-type recipients transplanted with empty vector (EV) or thrombopoietin-overexpression (TPO-OE) bone marrow (BM) 7 weeks after transplantation. Scale bar = 500 µm. **(B)** Analysis of bone marrow composition using Marrowquant in H&E-stained EV and TPO-OE femurs. EV $n = 3$, TPO-OE $n = 5$. **(C)** Number of adipocytes in H&E-stained EV and TPO-OE femurs. EV $n = 3$, TPO-OE $n = 5$, t-test for significance. **(D)** Representative overviews of H&E-stained biopsies from myeloproliferative neoplasm (MPN) patients with myelofibrosis Grade 0 (MF0) and MF3. Scale bars = 1 mm (overview image), 250 µm for zoom-in. **(E)** Quantification of total adipocyte area and number of adipocytes in a cohort of MPN patients with varying grades of fibrosis ($n = 11$ MF0; $n = 13$ MF1-3), unpaired t-test significance test, *P < 0.05. **(F)** Ridge plot showing aggregate expression of adipo- and osteo-genes per cluster (TPO vs. EV), two-sided Wilcox test. **(G)** Representative capture of microcomputed tomography (µCT) of tibia in mice transplanted with EV or TPO-OE overexpressing bone marrow 7 weeks post transplantation; scale bar = 1 mm. **(H)** Quantification of trabecular bone from µCT bones specifying bone volume over total volume and trabecular number. **(I)** Representative 3D reconstructions of the tibia in mice transplanted with EV or TPO-OE bone marrow, with trabecular thickness quantification shown. Color code represents the trabecular thickness in µm. Statistical significance is indicated by *P < 0.05, **P < 0.01, ***P < 0.001, and ****P < 0.0001.

confirmed by microcomputed tomography (μCT) analysis (Figure 5G–I). Bones in the fibrotic conditions had more bone, more trabeculae, and more trabecular connectivity, compared to the control (EV) condition (Figure 5H).

NCAM is a marker for fibrosis-driving cells in bone marrow fibrosis

We next applied sc2marker to identify specific markers to discriminate OLCs from FBs and CAR cells. The top markers identified were Fibulin (*Fbln1*) and *Ncam1* (CD56) (Figure 6A; Supporting Information S1: Figure 6A). However, *Fbln1* represented a less specific marker as it was expressed to some extent in FBs and CAR cells as compared to *Ncam1*, which was rather limited in its expression to OLCs and osteoblasts (Supporting Information S1: Figure 6A). In line with this, confocal imaging revealed a more unspecific pattern for fibulin expression (Supporting Information S1: Figure 6B). *Fbln1* was predominantly expressed in spindle-shaped cells with perivascular localization and diffusely beneath the GP in early stages of fibrosis, with increased expression surrounding Gli1;tdTom$^+$ cells in more progressed fibrosis. This might be explained by the fact that fibulin is known to integrate into fibronectin-containing matrix fibers, facilitating cell adhesion and migration along ECM protein fibers, thus indicating lower specificity to mark OLCs.[29]

To validate *Ncam1* as a marker for peritrabecular progenitor cells on the protein level, we stained murine BM for NCAM1 (Figure 6B). In the control (EV) condition, NCAM1$^+$ cells had a distinct localization just below the GP, seaming the osteogenic front toward the central marrow, in addition to surrounding trabeculae as spindle-shaped cells. In fibrosis (TPO-OE), NCAM1$^+$ cells significantly expanded from their peritrabecular localization (Figure 6C). In dense centers of NCAM1$^+$ cells, osteosclerosis was observed, and adipocytes were decreased, in line with the observed skewed differentiation of OLCs as peritrabecular mesenchymal progenitor cells.

Sc2marker further identified *Vcam1* (CD106) as a good discriminatory marker for CAR cells (Supporting Information S1: Figure 6C). The combined use of NCAM1 (CD56) and VCAM1 (CD106) allows for clear discrimination between OLC- and CAR-enriched populations, as these markers display distinct expression patterns as projected on the UMAP (Figure 6D). Flow cytometry confirmed that NCAM1 and VCAM1 can be used to differentiate between distinct stromal cell populations, and that the abundance of NCAM1$^+$ OLCs is increased in fibrosis, whereas there is a loss of VCAM1$^+$ CARs (Figure 6E,F). Flow cytometry further showed that NCAM1$^+$ cells are specifically enriched in the metaphysis while VCAM1$^+$ cells are ubiquitously distributed (Supporting Information S1: Figure 6D,E). To characterize these distinct populations better, we sort-purified and immortalized them for characterization by FACS and quantitative real-time reverse transcription PCR in vitro. Both NCAM1$^+$ and VCAM1$^+$ cells express typical stromal markers, as well as genes known to characterize stromal cells, such as the hematopoiesis-support genes *Cxcl12* and *Kitl* (Supporting Information S1: Figure 6F–H). In co-culture experiments with c-Kit$^+$ HSPCs, both NCAM1$^+$ and VCAM1$^+$ cells maintained a higher viability of c-Kit$^+$ HSPCs and decreased apoptosis compared to c-Kit$^+$ HSPC suspension culture without stromal support (Supporting Information S1: Figure 6F–J).

Having these discriminatory markers identified, we asked if the increased proliferation of NCAM1$^+$ OLCs (compare Figure 4B; Supporting Information S1: Figure 4C) can be validated. Combined Ki67 and NCAM1 staining confirmed the increased expression of Ki67 in NCAM1$^+$ cells lining the GP and located within nests of peritrabecular NCAM1$^+$ cells in the metaphysis. In addition, we observed Gli1;tdTom$^+$ NCAM1$^+$ spindle-shaped proliferates detaching from the trabecular bone and expanding into the interstitial space in BM fibrosis (Figure 6H), highlighting the cellular origin of NCAM1$^+$ OLCs in fibrosis.

To confirm the presence of peritrabecular OLCs in the human MPN disease setting, we stained control and MF patient samples for NCAM1 (Figure 6I). It is important to note that routinely taken diagnostic biopsies are from the pelvic region, which contains bone of trabecular quality. Using an automated digital pathology algorithm, we detected a significant increase in the overall area of NCAM1 staining, specifically in PMF patients (Figure 6J). In line with our murine data, NCAM1$^+$ cells were located "apposed to bone" (i.e., peritrabecular location) in healthy individuals. Importantly, there were distinct NCAM1 distribution differences between the MPN entities. NCAM1$^+$ cells were only found in high frequency in the central marrow (IT space) in the context of fibrosis in PMF, but not in MPN in general. To measure the fibrotic content in the patients' stainings, we computed the Continuous Indexing of Fibrosis (CIF) score and used the spatial distribution and heterogeneity of the CIF in individual patient slides[28] to obtain a principal components analysis (PCA) representation of our cohort (Figure 6K). The PCA discriminated patient samples of distinct entities and placed MF opposite to non-reactive (healthy) samples. Strikingly, when plotting the CIF score versus the "NCAM1 away from bone/NCAM1 total," MF patients and pre-MF patients formed a distinct group. This validates the fact that the spatial distribution of NCAM1$^+$ cells represents a solid marker for the different stages of fibrosis. It further highlights the potential of this readily available immunostain to identify patients in whom there is significant expansion/prominence of the NCAM1$^+$ endosteal lining cells in the context of (osteo)myelofibrosis.

Wnt signaling is upregulated in metaphyseal stromal progenitor cells and CAR cells

We next wondered if OLCs, as the peritrabecular progenitor cell reservoir for fibrosis-driving cells, can be therapeutically targeted. We thus investigated the molecular mechanisms that drive the activation of the stromal stem and progenitor cells in BM fibrosis with a focus on cell–cell interactions (CCI) using CrossTalkeR.[30] As hematopoietic cells are the fibrosis-inducing cells and contribute to the inflammatory niche, we included hematopoietic cells in the analysis to not lose any disease-relevant signals (Neutrophils 1, 2 and hematopoietic progenitors). In line with our hypothesis that CAR cells in the diaphyseal localization are reprogrammed by the fibrosis-inducing hematopoietic cells, the most significant interactions occur between all CAR cell clusters and hematopoietic cells. Hematopoietic cells also showed increased interaction with FBs, in line with their expansion throughout the marrow. IFN-CAR cells had significant interactions with OLCs, indicating that this subset is a main communicator in the fibrotic marrow (Figure 7A). We specifically looked into "chemokine" and "ECM regulator" interactions as drivers of BM fibrosis (Supporting Information S1: Figure 7A,B). As expected, the most pronounced chemokine-driven interactions occurred in the diaphysis (perivascular niche) between hematopoietic cells and CAR cells, specifically IFN_-CAR and CAR4_Pdg, but also in the metaphysis (trabecular niche) (OLC1/2). For the "ECM regulator"-dominated cross-talk, the main communication occurred between diaphysis and metaphysis, specifically between IFN_CAR and OLC2/3, and FBs, stressing the essential role of these populations in the fibrotic transformation.

Owing to the importance of OLC3 as a metaphyseal progenitor cell, we focused on OLC3-related receptor–ligand interactions and performed GO pathway analysis (Figure 7B). We identified central disease-relevant pathways in BM fibrosis, including integrin-mediated signaling, toll-like receptor signaling, platelet-derived signaling, and TGFβ receptor signaling,

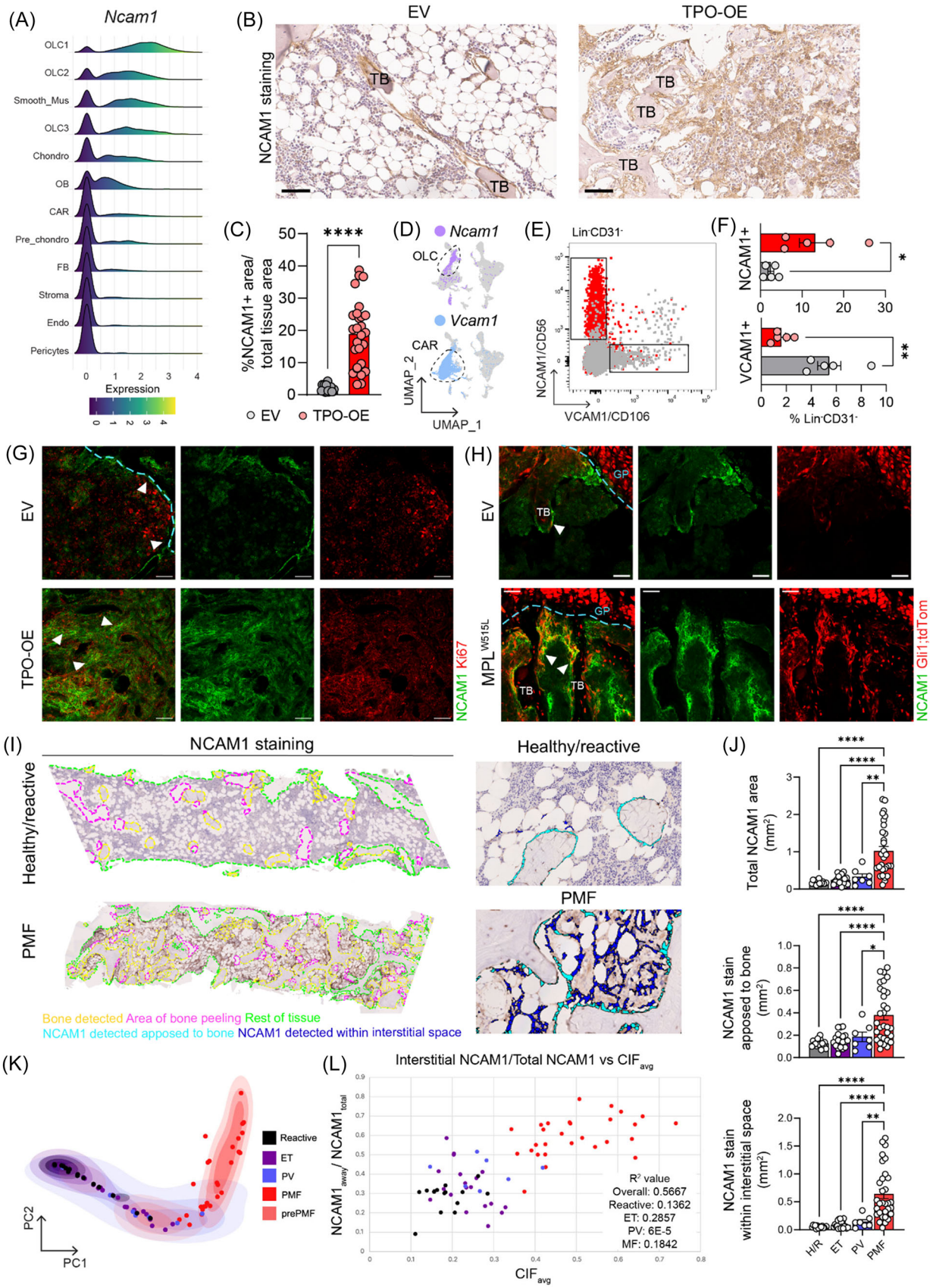

FIGURE 6 (See caption on next page).

FIGURE 6 **NCAM is a marker for fibrosis-driving cells in bone marrow fibrosis. (A)** Ridge plot of *Ncam1* expression for clusters. Clusters are ordered by mean *Ncam1* expression values. **(B)** Immunohistochemical staining of NCAM1 in murine biopsies from control (empty vector, EV) or fibrotic (thrombopoietin-overexpression, TPO-OE) bone marrow (BM). Scale bar: 50 µm (40×). TB, trabecular bone. **(C)** Quantification of NCAM1/CD56 staining in murine sections, one point represents the average stained area of three areas in murine bone, EV $n = 5$, TPO-OE $n = 9$, unpaired *t*-test. **(D)** UMAP showing cells expressing *Ncam1* > 2 and *Vcam1* > 2, dotted lines related to global osteolineage cell (OLC) and CXCL12-abundant reticular (CAR) clusters, respectively. **(E)** Representative fluorescence-activated cell sorting (FACS) plots of lineage negative, CD31 negative BM and digested bone chip (BC) from transplanted mice at harvest, NCAM1/CD56 and VCAM1/CD106 gates shown. **(F)** Quantification of NCAM1$^+$/CD56 and VCAM1$^+$/CD106 populations from cohort in (E). Unpaired *t*-test. **(G)** Representative confocal imaging of murine humeri, NCAM1/CD56 in yellow, Ki67 proliferation marker in red, scale bar = 50 µm. **(H)** Representative confocal imaging of murine humeri in Gli1;tdTom reporter, NCAM1/CD56 in yellow, Gli1;tdTom in red, scale bar = 50 µm. **(I)** Overview of healthy/reactive and primary myelofibrosis (PMF) patient bone marrow biopsy with annotated areas as indicated (left). The images on the right show, in magnification, the detected and quantified areas. **(J)** Quantification of NCAM in human biopsies as seen in (I). Healthy/reactive (H/R) $n = 15$, essential thrombocythemia (ET) $n = 19$, polycythemia vera (PV) $n = 7$, and PMF $n = 31$ samples. One-way analysis of variance (ANOVA) with multiple comparisons. **(K)** Principal component analysis (PCA) plot of the whole cohort using average image tile Continuous Indexing of Fibrosis (CIF) score, tile distribution, and heterogeneity of tile distribution as variables, as previously described.[28] **(L)** Association between CIF (*x*-axis) and NCAM1/CD56 (*y*-axis) cell expansion (defined by NCAM1 staining in interstitial space/total NCAM1 staining). Statistical significance is indicated by *P < 0.05, **P < 0.01, ***P < 0.001, and ****P < 0.0001.

and, in particular, a distinct Wnt-pathway signature. Filtering the CCI-plot for Wnt-pathway receptor–ligand pairs, Wnt-specific upregulation in the communication was noted in OLCs, CAR cells, and FBs (Supporting Information S1: Figure 7C). Specifically in fibrosis, OLC3 and broadly CAR cells showed a significant increase in the expression of the intracellular signal transducer of the Wnt pathway, β-catenin (*Ctnnb1*), as well as a decrease in expression of Wnt inhibitors *Sfrp1* and *Sfrp4* (Figure 7C).

Before exploring the relevance of targeting Wnt signaling in BM fibrosis, we aimed to validate the increased β-catenin signature in CAR cells and OLC3 in Gli1;tdTom$^+$ cells in BM fibrosis induced by the MPLW515L mutation. While in control BM, β-catenin expression was mostly limited to either cells lining the GP (Figure 7D), or to chondrocytes of the GP (Supporting Information S1: Figure 7B), the expression increased in expanding Gli1;tdTom$^+$ cells in the metaphysis in BM fibrosis (Figure 7D; Supporting Information S1: Figure 7E). We next asked if Wnt/β-catenin is differentially expressed in the BM stroma in patient samples. In control BM biopsies, β-catenin expression was limited to hematopoietic cells while spindle-shaped bone-lining cells did not stain positively (Figure 7E). We termed this stromal β-catenin Grade 0 (s-bCG0; Supporting Information S1: Figure 7F). In low-grade fibrosis, almost all bone-lining cells expressed β-catenin (s-bCG1). In progressing fibrosis, all bone-lining cells expressed β-catenin and started to extend from the bone (s-bCG2). The grading of the s-bCG confirmed a significant increase of the s-bCG with progressed fibrosis, although interestingly, the overall BM expression of β-catenin, also taking hematopoietic cells into account, rather showed a decrease with MPN and fibrosis progression (Supporting Information S1: Figure 7F).

Wnt signaling activation in the stromal compartment is a druggable target, and its inhibition ameliorates bone marrow fibrosis

Given that the Wnt pathway is specifically active in peritrabecular mesenchymal progenitor cells that are activated in fibrosis, we tested the effect of Wnt inhibition on fibrosis and osteosclerosis. Canonical Wnt signaling orchestrates skeletal regeneration upon injury,[31,32] so we hypothesized that its inhibition would keep OLCs uncommitted, halting their activation cycle. To this end, we repurposed Wnt inhibitors from cancer research, focusing on stabilizing the β-catenin destruction complex. We identified the Food and Drug Administration (FDA)-approved drug pyrvinium-tosylate (PT), which activates casein kinase 1α (CK1α), thereby promoting β-catenin degradation through phosphorylation, ubiquitination, and proteasomal pathways.

To provide proof-of-concept that the inhibition of the Wnt pathway with PT has therapeutic and translational relevance in the fibrotic transformation, we started twice-weekly treatment of mice under fibrotic (TPO-OE) or control (EV) conditions in three independent experiments (Supporting Information S1: Figure 8A). At harvest, we confirmed complete BM donor reconstitution in all groups (Supporting Information S1: Figure 8B). In the control conditions (EV-PBS and EV-PT), the blood parameters and BM morphology of EV-PBS and EV-PT mice did not differ (Supporting Information S1: Figure 8C–E), indicating that PT treatment does not have major effects on the hematopoietic system, as shown previously.[33]

In fibrosis, PT treatment also did not have major effects on myeloproliferation, although there was a trend of lower platelets and WBCs (Supporting Information S1: Figure 8C). The PT-treated TPO-OE mice also had a trend of higher BM cellularity (Supporting Information S1: Figure 8D) and a trend of smaller spleens (Supporting Information S1: Figure 8F). Strikingly, the reticulin fibrosis grade was significantly reduced in PT-treated compared to phosphate buffered saline (PBS) control TPO-OE mice (Figure 8A). Furthermore, the spleen morphology of PT-treated TPO-OE mice was less disturbed, indicating less progressed MPN disease (Supporting Information S1: Figure 8G). Importantly, we did not find major changes in HSC populations upon PT treatment, neither in EV nor in TPO-OE conditions (Supporting Information S1: Figure 8H).

To demonstrate that the effect of Wnt inhibition by PT treatment was mostly on CAR cells and to a lesser extent on HSCs, we performed scRNA sequencing of the BM after PT treatment compared to the PBS control and enriched for HSPCs and stromal cells (Figure 8C). We detected 11,063 cells (average 26,662 genes per cell), including major hematopoietic cell types as well as stromal cells (AdipoCar, OsteoCar, and OLCs), which we annotated by comparison with our tdTom$^+$ stromal clusters (Supporting Information S1: Figure 8I). *Col1a1* expression was significantly reduced in adipo- and osteo-CAR cells upon PT treatment (Figure 8D). The Wnt inhibitors *Sfrp1* and *4*, which we identified to be significantly reduced in fibrosis (compare Figure 7C) in adipo- and osteo-CAR cells, were significantly increased in these populations upon PT treatment but not in HSCs (Figure 8D; Supporting Information S1: Figure 8J). Comparing the mean expression of chondro-, adipo-, and osteo-associated gene sets also confirmed the upregulation of chondro- and osteo-gene sets in TPO-OE-PBS and an upregulation of the adipo-gene sets upon PT treatment (Figure 8E). These results, that is, increase of Wnt inhibitor genes and normalization of stromal skewing signatures in CAR cells, support the direct effect of the PT treatment in the stromal compartment. Concordantly, the frequency of NCAM1$^+$ cells throughout the BM was significantly reduced in TPO-OE transplanted mice after PT treatment compared to PBS-treated controls (Figure 8F,G).

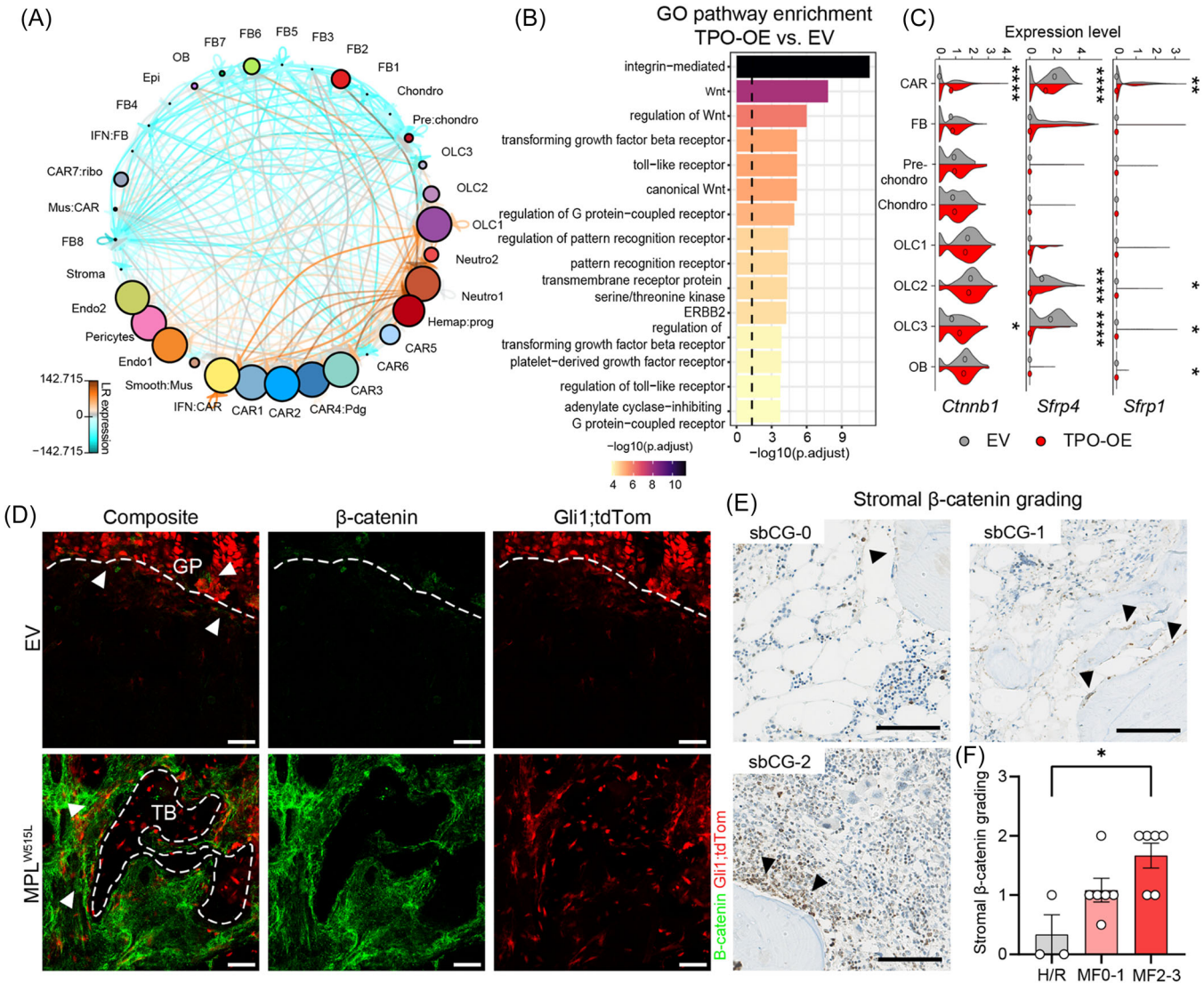

FIGURE 7 **Wnt signaling is activated in OLC3 in bone marrow fibrosis**. **(A)** Cell–cell interactions (CCI) plot signaling showing ligand–receptor (LR) interactions of the different niches (metaphysis, diaphysis, transition vs. hematopoietic = hemap) and cell clusters (thrombopoietin-overexpression [TPO-OE] vs. empty vector [EV]). The size of a cell indicates its importance in the CCI network. The thickness of the edges indicates the number of LR interactions, while the color indicates the relative change in expression (orange is higher in TPO-OE and blue is higher in EV). **(B)** Gene ontology (GO) enrichment of the enriched LR pairs with expression in TPO-OE versus EV in the OLC3 cluster using ClusterProfiler. **(C)** Violin plot depicting the Wnt modulator *Ctnnb1* and inhibitors *Sfrp1* and *Sfrp4*, median depicted with a circle; Wilcoxon test for significance, only significant results shown. **(D)** β-Catenin staining of murine humeri, EV = control, MPLW515L = fibrotic marrow. A composite image is shown, and the right panels show individual channels of β-catenin and Gli1;tdTom, respectively. White arrowheads highlight β-catenin and Gli1;tdTom co-expression. Scale bar = 50 μm. **(E)** Representative immunohistochemical staining of β-catenin, each panel showing stromal β-catenin grades 0–2. Scale bar: 100 μm. **(F)** Stromal β-catenin grading (sbCG) of human bone marrow biopsies, and one-way analysis of variance (ANOVA) with Kruskal–Wallis. H/R, healthy/reactive; MF, myelofibrosis/reticulin grades 0–3. Statistical significance is indicated by *P < 0.05, **P < 0.01, ***P < 0.001, and ****P < 0.0001.

NCAM1^{+} cells were solely found in their peritrabecular localization, indicative of less activation of this population upon PT treatment.

To gain a spatial view of transcriptional changes occurring in PT-treated mice, we performed spatial transcriptomic experiments in nine bones (3x EV_PBS, 3x TPO-OE_PBS, 3x TPO-OE_PT) using the Visium platform (Figure 8H–J). We captured a total of 5250 spots with an average recovery of 2644 genes per spot. Unsupervised clustering identified eight spatial domains (SpDs) (Figure 8K,L). The majority of the dataset was represented by SpDs consisting of a mixture of CD45^{+} (*Ptprc* expressing) hematopoietic cells and Cxcl12-expressing stromal cells (Figure 8K,L) within the BM. The megakaryocyte (MK)-fibroblast (Fib)-endothelial (endo) SpD and the MK_CAR SpD mapped to the central marrow, while the MK_OLC SpD mapped to the GP, trabecular region, and cortical bone of the diaphysis. The chondrocyte (chondro) SpD aligned with the GP and other stromal populations were scattered across the bone (Figure 8J). We observed particularly high expression of platelet factor 4 (*Pf4*), commonly expressed in monocytes, macrophages, and megakaryocytes, in a number of SpDs (Supporting Information S1: Figure 8K).

The most significant ECM-associated transcriptional reprogramming occurred in the MK_CAR and MK_Fib_Endo SpDs in BM fibrosis, particularly with regard to NABA collagens (Figure 8M). Strikingly, PT treatment significantly decreased collagen expression in these SpDs

compared to TPO-OE vehicle-treated animals (Figure 8N). In line with our previous findings, we found increased Wnt-pathway gene expression in the MK_CAR and MK_Fib_Endo populations in TPO-OE bones compared to controls (Figure 8O; Supporting Information S1: Figure 8L). Furthermore, these SpDs had an increased chondrogenic, as well as osteogenic signature in fibrosis (Figure 8P,K; Supporting Information S1: Figure 8L), highlighting the calcification and osteogenic differentiation stromal switch occurring in BM fibrosis. These were also significantly reduced upon PT treatment, supporting the notion that PT treatment prevents the stromal skewing in fibrosis and normalizes the stromal differentiation (Figure 8O–Q), as also observed in the scRNAseq data (Figure 8E). We thus identified in an unbiased fashion a disease- and fibrosis-inducing cell-specific pathway, which can be targeted by repurposing an FDA-approved drug with a known safety profile.

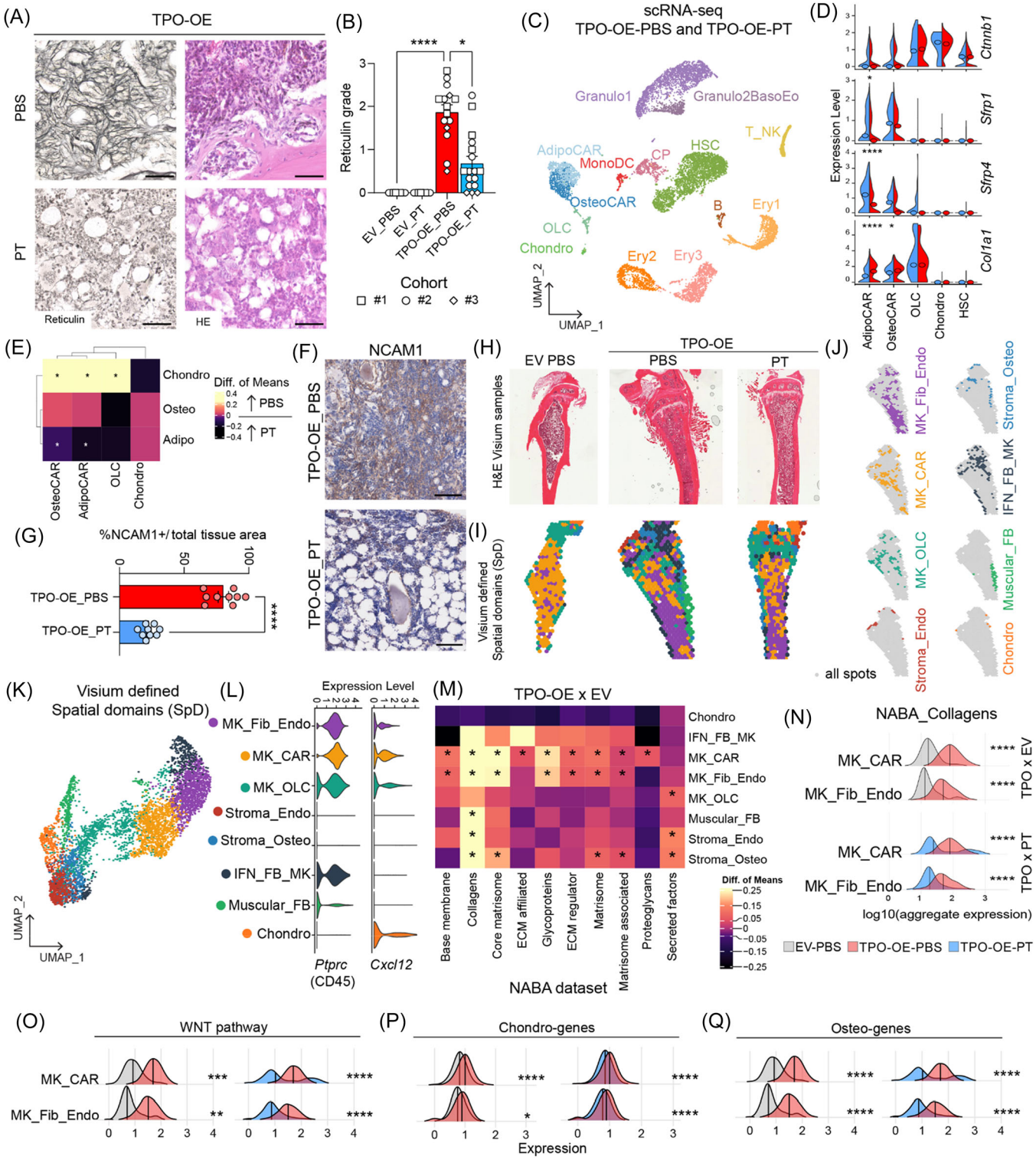

FIGURE 8 (See caption on next page).

FIGURE 8 **Inhibition of Wnt signaling reduces fibrotic transformation and osteoclerosis in bone marrow (BM) fibrosis. (A)** Representative reticulin and hematoxylin and eosin (H&E) staining of tibias of BM transplant of c-Kit-enriched cells transduced with empty vector (EV)-eGFP (EV) or thrombopoietin-overexpression (TPO-OE)-eGFP (TPO-OE) viral vector and treatment with pyrvinium-tosylate (PT)-dimethyl sulfoxide (DMSO) solution (PT) or phosphate buffered saline (PBS)-DMSO (PBS) as a control. Scale bar: 50 µm. **(B)** Reticulin grade according to the World Health Organization (WHO). Kruskal–Wallis rank test. EV-PBS $n = 8$, EV-PT $n = 8$, TPO-PBS $n = 15$, and TPO-PT $n = 17$; three independent cohorts; shape of points refers to cohort. **(C)** UMAP of single-cell RNA sequencing (scRNAseq) dataset of lineage-depleted BM and collagen-digested bone chip fractions (digBC) of TPO-PBS and TPO-PT mice, $n = 3$ mice pooled per experimental group. $N = 11{,}063$ cells. **(D)** Violin plot depicting the Wnt modulator *Ctnnb1* and inhibitors *Sfrp1*, *Sfrp4*, and *Col1a1* expression in stromal populations and HSCs. Median depicted with a circle, the Wilcoxon test for significance. One-sided Wilcoxon test. **(E)** Heatmap of differences of mean expression of adipo-, osteo-, chondro-gene sets per stromal cluster from panel (O), TPO-OE_PBS compared to TPO-OE_PT. One-sided Wilcoxon test. **(F)** Representative immunohistochemistry of NCAM1 in femurs of TPO-PBS and TPO-PT-treated mice, space bar = 100 µm. **(G)** Quantification of NCAM1 staining shown in (M), $n = 3$ mice per experimental group, quantification of three areas per slide, unpaired *t*-test. **(H)** H&E of tibias used for Visium spatial transcriptomics, $n = 3$ per group, one representative image shown per experimental group. **(I)** Visualization of spatial domains (SpDs) detected in tibias as defined in (E). **(J)** Individual SpDs are shown in respective cluster colors with the TPO-PBS bone as a representative example. **(K)** UMAP of SpD clusters identified by Visium spatial transcriptomics. **(L)** VlnPlots of *Cxcl12* and *Ptprc* (CD45) expression per SpD. **(M)** Heatmap of differences of mean expression of NABA gene sets per identified SpD, TPO-PBS compared to EV-PBS. One-sided Wilcoxon test used. High difference of mean expression represents higher expression in TPO-PBS compared to EV-PBS and vice versa. **(N)** Ridge plot showing aggregate expression of NABA collagen genes per identified SpD. Two-sided Wilcox test performed per SpD cluster, per comparison. One-sided Wilcoxon test was used to assess the statistical significance of the distribution differences. **(O–Q)** Ridge plot showing aggregate expression of Wnt signaling pathway genes (O), chondro-genes (P), osteo-genes (Q) per SpD. TPO-OE PBS versus EV PBS in the left panel, and TPO-OE PT versus TPO-OE PT in the right panel. Two-sided Wilcox test performed per SpD cluster, per comparison. Rest of SpDs shown in Supporting Information S1: Figure 8J. Statistical significance is indicated by *P < 0.05, **P < 0.01, ***P < 0.001, and ****P < 0.0001.

DISCUSSION

There is increasing evidence that fibrotic processes across different organs are a result of a dysregulated repair response following repeated tissue injury, most notably during chronic inflammatory disorders.[2,3,19,34] BM fibrosis is the most extensive remodeling of the BM and is most commonly initiated by the presence of mutated hematopoietic cells in MPNs, resulting in a reactive, cytokine- and chemokine-driven microenvironment. Previously, Gli1$^+$Lepr$^+$ adipogenic- and osteogenic-CAR cells were shown to be functionally reprogrammed into fibrosis-driving cells in the presence of a fibrosis-inducing hematopoietic clone.[8,11,35,36] However, spatial information on how the distinct anatomical regions of the bone are differentially affected was missing, as either spatial resolution was not available or only the central marrow was taken into account. By combining fate tracing using three mesenchymal Cre-reporters, whole-mount bone imaging, and single-cell RNA sequencing, we now demonstrate a well-orchestrated interplay between the central marrow (perivascular niche) and the endosteal niche, with a focus on trabecular bone in fibrosis, with high resemblance to skeletal repair involving the Wnt-mediated activation of a peritrabecular mesenchymal progenitor cell.

Our data indicate that the injury stimulus predominantly occurs in the central, perivascular BM niche, in line with recent reports.[8,11,35,36] The central (perivascular) niche harbors 85% of HSPCs, including the mutated or fibrosis-inducing clone.[37] Perisinusoidal and periarterial CAR cells, which mapped back to the central niche of the diaphysis, were functionally reprogrammed, lost hematopoiesis-supporting capacity, and acquired a pro-inflammatory phenotype as a result of their increased communication with fibrosis-inducing hematopoietic cells. Importantly, CAR cells showed a distinct phenotypic switch while leaving their perivascular niche and invading the central marrow. We provide evidence that true CAR cells are progressively lost during the fibrotic transformation through the upregulation of apoptosis, and that their frequency is reduced. The absence of CAR cells in the direct association with endothelial cells exposes the endothelium to the inflammatory environment. Endothelial cells (Endo-1) showed transcriptional changes consistent with endothelial-to-mesenchymal transition. Apelin is a marker for H-vessels, which represent the endothelium-bone axis and maintain the cross-talk of the metaphyseal and central BM niche.[24] In the context of our data, the upregulation of Apelin can be considered to promote increased communication and changes in the quality of the endothelium, which coordinate the injury response of the perivascular central niche to the endosteal niche.

Within the metaphyseal region, stromal cells in close association with trabecular bone are a reservoir for fibrosis-driving cells in BM fibrosis. Cells residing in the peritrabecular region expand in a stepwise fashion during fibrosis and have a higher colony-forming potential compared to diaphyseal cells, indicative of a progenitor cell state. We propose that a subset of osteolineage cells, specifically OLC3, is activated in an injury-specific fashion, acts as a mesenchymal progenitor, and is enriched in the Gli1-Cre lineage traced cells in BM fibrosis. This was of particular interest as Gli1$^+$ cells were previously identified as an osteogenic progenitor for fracture repair and termed "metaphyseal mesenchymal progenitors." This postnatal Gli1$^+$ cell pool with multi-lineage potential, immediately beneath the GP, is essential for skeletal repair, but remains mostly quiescent in the adult mouse.[5,12] Importantly, we previously demonstrated that genetic ablation of Gli1$^+$ cells rescues the fibrotic transformation of the BM, proving their functional relevance in fibrosis.[5] Our data now indicate that OLCs are skewed toward chondrogenesis and ossification (leading to osteosclerosis) and show increased differentiation into FBs, which are expanded in BM fibrosis. Ly6a$^+$-FBs express high levels of collagens at baseline and acquire an inflammatory phenotype, consistent with their behavior as first responders to injury in solid organs. So far, FBs were underrepresented and poorly described in BM fibrosis single-cell datasets, most likely due to the focus of previous reports on the central marrow.[8,35] We identified NCAM1 as a marker for OLCs, which are expanded in fibrotic marrow, and correlate with fibrosis severity in PMF patients.

Functional differences between the perivascular and endosteal niche were also described during normal hematopoiesis, quite in line with our findings. The perivascular (sinusoidal) niche mostly reacts to injury,[38] while the endosteal niche is important in regeneration. We demonstrate that mesenchymal progenitor cells with colony-forming potential are enriched in the metaphysis (peritrabecular region), in line with previous reports that perisinusoidal CAR cells are rather quiescent but have abundant cytokine expression[31] and that metaphyseal mesenchymal cells have self-renewing and multi-lineage differentiation potential.[25] Peritrabecular regions are thus a hot spot of fibrosis formation and are activated in an injury-like fashion.

Based on our findings, the optimal anti-fibrotic treatment in the BM would target not only processes in the central marrow but also the peritrabecular progenitor cell. Receptor–ligand interactions demonstrated that OLCs are tightly regulated by Wnt signaling, in line with previous reports showing Wnt-mediated osteogenic transformation of BM stromal progenitors in skeletal regeneration.[31] Injury-induced Wnt signaling can drive mesenchymal progenitor cells into a reticular-osteoblast hybrid

state, and β-catenin signaling was shown to be a driver but also therapeutic target in solid organ fibrosis,[32] thus linking fibrosis and osteogenesis upon injury. Our data show that Wnt signaling is also upregulated in the myeloproliferative (non-fibrotic) phase in hematopoietic cells, but fibrosis specifically correlates with stromal expression of β-catenin in a disease-specific fashion. This is in line with recent studies identifying a TGFβ-Wnt-HOXB7 axis as associated with a profibrotic and pro-osteoblastic biased differentiation of mesenchymal stromal cells isolated from patients, making this pathway an attractive target.[39] Importantly, Wnt-mediated stromal cellular communications were mostly active in disease but not under steady state conditions, highlighting the potential to specifically target the diseased cells. Repurposing of PT as a potentially clinically relevant compound that acts as an activator of casein-kinase 1a (CK1a or CSNK1a1) had anti-fibrotic effects and abolished osteosclerosis, restored the skewed differentiation of stromal cells in fibrosis, leading to the preservation of hematopoiesis. We demonstrated by scRNA sequencing that PT treatment affects predominantly (non-canonical) Wnt signaling in stromal populations. Previous studies have, however, also shown a positive effect of MPN in general with other Wnt inhibitors, mostly reducing platelet counts,[40] suggesting that targeting Wnt has positive effects not only on myeloproliferation but also on the fibrotic reprogramming of the stroma. We thus identified in an unbiased fashion a disease-, osteosclerosis- and fibrosis-inducing cell-specific pathway, which can be targeted by repurposing an FDA-approved drug with a known safety profile.

MATERIALS AND METHODS

Animal studies

All mouse studies were conducted according to protocols approved by the Central Animal Committee (Centrale Commissie Dierproeven [CCD], the Netherlands) in accordance with legislation in the Netherlands (Approval No. AVD1010020173387 and AVD2216373). Mice were maintained on a 12-h light/dark cycle and were provided with water and standard mouse chow ad libitum. Mice were randomly assigned to experimental groups.

PtprcaPepcb/BoyCrl (B6.SJL) and C57BL/6J mice were purchased from Charles River (the Netherlands) and maintained in specific-pathogen-free conditions. Gli1CreERt2 (Gli1tm3(re/ERT2)Ali/J, JAX Stock #007913), Pdgfrb-creERt2 (B6-Cg-Gt(Pdgfrb-cre/ERT2)6096Rha/J), Rosa26tdTomato (B6-Cg-Gt(ROSA)26Sorttm(CAG-tdTomato)Hze/J, JAX Stock #007909), Ly6a-eGFP (B6.Cg-Tg(Ly6a-EGFP)G5Dzk/J, JAX stock #012643), and Grem1-creERT (B6.Cg-Tg(Grem1-cre/ERT)3Tcw/J, JAX stock #027039) were purchased from Jackson Laboratories (Bar Harbor, ME, USA). Offspring were genotyped by PCR according to the Jackson Laboratory protocol. For lineage tracing, 10–15 week old mice were injected intraperitoneally with 4 × 3 mg tamoxifen in corn oil/3% ethanol (Sigma) at least 21 days before BM transplantation. Unless otherwise specified, both male and female mice were used.

Viral transduction for bone marrow transplant

Lentiviral particles were produced by transient transfection with lentiviral plasmid together with pSPAX and VSVG packaging plasmids using TranIT (Mirus) and concentrated by ultracentrifugation at 4°C for 2 h. For lentiviral transduction, CD117(c-Kit)-enriched cells from donor mice were isolated by crushing hind legs and subsequent CD117-enrichment by magnetic separation (Miltenyi Biotec). c-Kit$^+$ BM cells were cultured in StemSpan media (Stem Cell Technologies) supplemented by murine stem-cell factor (m-Scf, 50 ng/mL, Peprotech) and murine thrombopoietin (m-Tpo, 50 ng/mL, Peprotech). c-Kit$^+$ cells were transduced with virus (empty vector, EV-eGFP or thrompoietin overexpression, TPO-eGFP) in the presence of polybrene (4 μg/mL) for 48 h, then transplanted into recipient mice in sterile saline solution.

Induction of myelofibrosis by overexpression of thrombopoietin (TPO)

Tamoxifen-induced recipient mice were irradiated with a split-dose regimen (2 × 6.02 Gy) and received c-Kit$^+$-enriched cells from non-tamoxifen-treated littermates harvested 48 h prior to transplantation and transduced with thrombopoietin-overexpressing (TPO-eGFP+) lentivirus or control empty vector lentivirus (EV-eGFP+). For the Ly6a-EGFP and WT recipient cohorts, wild-type (WT) c-Kit$^+$-enriched cells were transduced with thrombopoietin (TPO) or EV control lentivirus and transplanted into lethally irradiated (split-dose) B6.Cg-Tg(Ly6a-EGFP) G5Dzk/J (n = 5 mice per group) and B6.SJL recipient mice (n = 3–6 mice per group). Transplanted mice received drinking water supplemented with enrofloxacin (Baytril) for 3 weeks post-transplantation.

Blood was periodically collected via submandibular bleeds into microtainer tubes coated with K2EDTA (Becton Dickinson, NJ, USA), and complete blood counts were performed on a Horiba Scil Vet abc Plus hematology system. Mice were harvested when they showed signs of fibrosis, as indicated by a drop in hemoglobin levels or weight loss, according to defined humane endpoints. At harvest, long bones, pelvis, and spine were collected for BM analysis. Femurs were collected for imaging by fixing in 2% PFA for 10 h, stored in 30% sucrose/PBS, and processed further as described above/below.

In vivo treatment with pyrvinium-tosylate (PT)

PT salt (SY-pyrvinium) was purchased from Symansis (Timaru, New Zealand). The PT salt was first diluted in dimethyl sulfoxide (DMSO) at 10 mg/mL and stored at −80 °C in dark tubes, and subsequently diluted in PBS for i.p. injection twice weekly at a dose of 0.5 mg/kg (PT groups). Control mice receive equivalent dilutions of DMSO in PBS (PBS groups).

Histological and immunohistological analysis

Murine organs were fixed in 2% paraformaldehyde for 12 h and transferred to 70% ethanol. Spleens were weighed before fixation. Bones were decalcified in 0.5 M ethylenediaminetetraacetic acid (EDTA) for 6 days, dehydrated, and paraffin-embedded. Hematoxylin and eosin (H&E) and reticulin staining were performed on 4 μm sections according to established routine protocols.

Human BM biopsies were fixed for 24 h using the Hannover Solution (12% buffered formaldehyde plus 64% methanol), decalcified (EDTA), dehydrated, and embedded in paraffin. Immunohistochemical stainings for active b-catenin (05-665, clone 8E7, Sigma) were performed with an automated, validated, and accredited staining system (Ventana Benchmark ULTRA, Ventana Medical Systems, Tucson, AZ, USA) using optiview universal DAB detection Kit (#760-700). In brief, following deparaffinization and heat-induced antigen retrieval, the tissue samples were incubated with mouse anti-active-β-catenin for 16 min at 36°C. Incubation was followed by hematoxylin II counterstain for 12 min and then a blue coloring reagent for 8 min according to the manufacturer's instructions (Ventana). Slides were scanned and digitized in an automated fashion using a Hamamatsu Nanozoomer 2.0 HT system. Images were analyzed and exported using the NDP.view software (Hamamatsu, V2.5.19).

Processing and whole-mount imaging of bone

Methods for 3D imaging of BM were adapted from previously published protocols.[41] Mouse femurs were isolated, cleaned, and immersed in PBS/2% paraformaldehyde for 6 h, followed by a dehydration step in 30% sucrose for 72 h at 4°C. Femurs were then embedded in cryopreserving medium (OCT) and snap frozen in liquid nitrogen. Bone specimens were iteratively sectioned using a cryostat until the BM cavity was fully exposed along the longitudinal axis. The OCT block containing the bone was then reversed, and the procedure was repeated on the opposite face until a thick bone slice with bilaterally and evenly exposed BM content was obtained. Once the BM slices were generated, the remaining OCT medium was removed by incubation and washing of the bone slices in PBS three times for 5 min. For immunostaining, slices were incubated in blocking solution (0.2% Triton X-100, 1% BSA, and 10% donkey serum in PBS) overnight at 4°C. Primary antibody immunostainings were performed in blocking solution for 3 days at 4°C, followed by overnight washing with 0.2% Triton X-100 in PBS. Secondary antibody staining was performed for another 3 days at 4°C in blocking solution but in the absence of BSA to avoid cross-absorption. Immunostained thick femoral slices were successively washed overnight with 0.2% Triton X-100 in PBS and incubated in RapiClear 1.52 overnight. For observation under the confocal microscope, BM slices were mounted on glass slides while embedded in RapiClear. Confocal microscopy was performed with 10× (HCX PL FLUOTAR), 20× (HC PL APO CS2), and 63× (HCX PL APO CS2) in Leica STELLARIS 5 equipped with a 405-nm laser, white light laser, and hybrid detectors. Confocal image stacks were processed and rendered into a three-dimensional volume on Imaris Software (Oxford Instruments, UK).

Isolation of BM stromal cells for scRNA sequencing

Femurs, tibiae, hips, and spines were dissected and cleaned of surrounding tissue as much as possible. The bones were crushed in 2% fetal calf serum (FCS)/PBS using a mortar and pestle. Dissociated cells were filtered through a 70-µm nylon cell sieve, spun down, and lysed with PharmLyse RBC lysis buffer. The cells were lineage-depleted using biotinylated antibodies directed against lineages (CD5, CD45R, CD11b, Gr1, 7-4, Ter119) (Miltenyi Biotec) and additionally added CD45- and CD71-biotin antibodies (Biolegend). After staining for 10 min at 4°C, the cells were washed and incubated with anti-biotin beads (Miltenyi biotec) for 15 min at 4°C prior to magnetic depletion using an MACS column (BD).

For the isolation of cells from bones, crushed BCs were washed with 2% FCS/PBS, and incubated with 10 mL of Collagenase II (1 mg/mL) at 37°C for 45 min under gentle agitation. The cell suspension was strained through a 70-µm nylon cell sieve, spun down, and lysed with PharmLyse RBC lysis buffer before being pooled with the lineage-depleted BM fraction described above.

FACS-staining and sorting of bone marrow stromal cells for scRNA sequencing

Cells were resuspended in 300 µL PBS/2% FCS and stained at 4°C for 20 min with the antibodies described below. Washing was performed by adding 1 mL PBS/2% FCS and centrifuging for 5 min at 300 × *g*, 4°C. After resuspension and addition of Hoechst (1:10,000), lineage/CD45/CD31 negative, tdTom positive cells were sorted into 400 µL PBS/10% FCS (BD Aria III) and used as input for the 10× platform. A fully stained sample from a tdTom-negative mouse served as a negative control to define tdTomato gating. All antibodies were acquired from Biolegend. The following fluorochrome-conjugated antibodies were used for murine samples: CD41-APC-Cy7, CD3-APC-Cy7, CD11b-APC-Cy7, Gr1-APC-Cy7, Ter119-APC-Cy7, B220-APC-Cy7, CD45.1-APC-Cy7, CD45.2-APC-Cy7, and CD31-APC.

For non-tdTomato samples, TPO_PBS versus TPO_PT datasets, the same tissue processing as described above was performed, after which the sample was sorted for stromal (lineage/CD31/c-Kit/CD45/GFP negative alive singlets), and LSK events (lineage negative c-Kit$^+$Sca1$^+$ alive singlets). The stromal and LSK fractions were pooled in a 5:1 ratio and loaded onto the 10X chip. All antibodies were acquired from Biolegend. The following fluorochrome-conjugated antibodies were used for murine samples: CD41-APC-Cy7, CD3-APC-Cy7, CD11b-APC-Cy7, Gr1-APC-Cy7, Ter119-APC-Cy7, B220-APC-Cy7, CD71-APC-Cy7, Sca1-PerCP, c-Kit-PeCy7, CD45.1-FITC, CD45.2-FITC, and CD31-PE-CF594.

Methocult (CFU-assay) of LSK-sorted cells after PT treatment in vivo

A total of 1500 primary, prospectively sorted LSK cells (lineage negative c-Kit$^+$Sca1$^+$ alive singlets) were plated out per 1 mL Methocult GF M3434 + 1% P/S in triplicate, with three biological replicates per experimental group. Plates were counted after 7 days.

Culturing of bone marrow-derived stromal cells

Digested BCs were washed thoroughly to remove hematopoietic contamination and cultured in full medium (alpha-MEM [Lonza], 20% FCS, 1% penicillin/streptomycin, 1 ng/mL murine bFGF [Peprotech], and 5 ng/mL murine EGF [Peprotech]) under normoxic conditions. After 9 days, the BCs were discarded. Attached culturing of bone marrow-derived stromal cells (cBMSCs) were passaged every 3–5 days at approximately 80% confluence, and CD45/CD11b expression was assessed before the start of the experiment.

Prospective sorting of stromal cells for CFU-F assays from metaphysis and diaphysis of long bones

Femurs, tibias, and humeri were cleaned thoroughly, removing all muscle and tendons, and the periosteum was scraped using a small scalpel blade to remove potentially contaminating periosteal stromal cells. The intact long bones were digested using trypsin (2.5 mg/mL) and Collagenase II (2 mg/mL) for 20 min at 37°C, rinsed with PBS, and scraped to remove any remaining periosteum. Long bones were cut into metaphysis and diaphysis and subsequently processed as separate samples (Meta/Dia). The bones were crushed in 2% FCS/PBS using a mortar and pestle. Dissociated cells were filtered through a 70-µm nylon cell sieve, spun down, and lysed with PharmLyse RBC lysis buffer. The BC fractions were digested with Collagenase II (1 mg/mL) for 45 min at 37°C, then washed with 2% FCS/PBS, before combining with the respective BM fractions. Cells were stained for flow cytometry using anti-CD29, anti-CD31, anti-Sca1, anti-CD200, anti-VCAM1, anti-CD45, anti-Ter119, anti-B220, anti-CD3, anti-CD11b, anti-Gr1, and Hoechst as a live/dead marker. PdgfrbCre- or Gli1Cre-lineage stromal cells were sorted on a FACSAriaIII as live, lineage-negative, CD31-tdTomato$^+$ cells and seeded in MesenCult Expansion kit (mouse, Stem Cell Technologies) according to the manufacturer's instructions.

Single-cell library preparation and sequencing

The libraries were prepared using the Chromium Next GEM Single Cell 3′ Reagent Kits (v3.1): Chromium Next GEM Single Cell 3′ GEM Kit v3.1 (PN-1000123), Chromium Next GEM Chip G (PN 2000177), Chromium Next GEM Single Cell 3′ Library Kit v3.1 (PN-1000157), Dual Index Kit TT Set A (PN-1000215), and following the Chromium Next GEM Single Cell 3′ Reagent Kits (v3.1) User Guide (manual part no. CG000315, Rev B). Finalized libraries were sequenced on a Novaseq. 6000 platform (Illumina), aiming for a minimum of 50,000 reads/cell using the 10X Genomics recommended number of cycles (28-8-0-91 cycles).

scRNAseq data analysis

The scRNAseq count matrix was obtained by aligning the raw sequencing reads into the custom tdTomato transcripts added mm10 mouse reference genome via the cellranger (version 4.0.0 and 6.0.1). Next, we used Seurat (v4.2) to analyze the scRNAseq[42] based on R version 4.2.1. We filtered out cells with a high amount of mitochondrial genes (>10%), cells with low (<200) or high feature counts (>4000), and removed the *Xist* gene to mitigate gender differences in downstream analyses. Next, we regressed out cell-cycle–related genes, the proportion of mitochondrial, ribosomal, and UMI counts, and performed a log-normalization of read counts. All scRNAseq libraries were integrated with Seurat's reciprocal PCA (RPCA) based on the first 30 PCs. Unsupervised clustering was performed with the Louvain resolution 1.4. We used the FindMarkers gene function with an adjusted P-value < 0.05 to find cluster-specific markers. Differential gene expression analysis was performed, showing changes between distinct phenotypes. For this, we considered only genes with an absolute fold change greater than 0.5 and adjusted P-value < 0.1. GO and pathway enrichment analysis was based on the EnrichR package, looking into the NABA gene set.[18] All P-values were corrected by Benjamini–Hochberg correction. DEGs, including corresponding statistics, are supplied in a table inside the folder for Figure 2 of the 08-11-2024 Zenodo repository.

scRNAseq analysis, histological stainings, and microCT analysis are described in detail in the Supporting Information S1: Supplemental Materials.

ACKNOWLEDGMENTS

We thank Remco Hoogenboezem for preprocessing the scRNA sequencing data; Stephani Schmitz, Aurélie van Kleef-Boeree, Iris Bakker, and Pia Wanner for technical support; Juliette Pearce for creating the graphical abstract; and the Developmental Biology department of Erasmus MC for helpful scientific discussions. We thank the team of the Laboratory Animal Science Center at Erasmus Medical Center, Rotterdam, for their technical assistance.

AUTHOR CONTRIBUTIONS

Bella Banjanin: Investigation; writing—original draft; methodology; validation; conceptualization; visualization; writing—review and editing; formal analysis. **James Nagai**: Conceptualization; investigation; methodology; writing—original draft; data curation; writing—review and editing; visualization; formal analysis; software. **YeVin Mun**: Investigation; methodology; writing—review and editing; formal analysis; resources. **Stijn Fuchs**: Investigation; methodology; validation. **Inge Snoeren**: Methodology; investigation; validation. **Joachim Boers**: Investigation; methodology; formal analysis; writing—review and editing. **Mayra L. Ruiz Tejada Segura**: Investigation; methodology; software. **Hector Tejeda Mora**: Methodology; investigation; validation. **Anna Katharina Galyga**: Investigation; validation. **Adam Benabid**: Investigation; writing—review and editing; validation. **Rita Sarkis**: Methodology; formal analysis. **Olaia Naveiras**: Methodology; formal analysis; supervision. **Marta Rizk**: Validation; investigation. **Michael Wolf**: Investigation; validation. **Rogerio B. Craveiro**: Investigation; validation. **Fabian Peisker**: Investigation; validation. **Ursula Stalmann**: Methodology; investigation. **Jessica E. Pritchard**: Methodology; validation; writing—review and editing. **Hosuk Ryou**: Validation; methodology; investigation; formal analysis. **Nasullah Khalid Alham**: Validation; methodology; formal analysis. **Marek Weiler**: Validation; methodology; resources. **Fabian Kiessling**: Methodology; validation; supervision; resources. **Twan Lammers**: Methodology; validation; supervision; resources. **Anna Rita Migliaccio**: Methodology; validation; writing—review and editing. **Kishor Kumar Sivaraj**: Methodology; validation; investigation. **Ralf H. Adams**: Methodology; validation; investigation; supervision. **Eric Bindels**: Validation; methodology. **Joost Gribnau**: Methodology; investigation. **Daniel Royston**: Validation; methodology; supervision. **Hélène F. E. Gleitz**: Validation; investigation; writing—review and editing; methodology. **Rafael Kramann**: Investigation; methodology; conceptualization; writing—review and editing. **César Nombela-Arrieta**: Conceptualization; investigation; validation; writing—review and editing; supervision; methodology. **Ivan G. Costa**: Writing—original draft; funding acquisition; conceptualization; supervision; formal analysis; writing—review and editing; investigation; methodology. **Rebekka K. Schneider**: Conceptualization; investigation; funding acquisition; writing—original draft; validation; supervision; methodology; writing—review and editing; project administration; resources; formal analysis.

CONFLICT OF INTEREST STATEMENT

The authors declare no competing interests directly related to this work. The authors, however, disclose the following unrelated funding, honoraria, and ownership: R.K.S. has a grant from Active Biotech. R.K. has grants from Travere Therapeutics, Galapagos, Chugai, and Novo Nordisk, and is a consultant for Bayer, Pfizer, Novo Nordisk, and Gruenenthal. I.G.C. has a grant from Illumina. R.K. and R.K.S. are founders and shareholders of Sequantrix GmbH.

DATA AVAILABILITY STATEMENT

The data that support the findings of this study are openly available in Zenodo at 10.5281/zenodo.8249674. The sequencing data are also available from Gene Expression Omnibus (GEO): GSE282516 (https://zenodo.org/records/14054131?token=eyJhbGciOiJIUzUxMiIsImlhdCI6MTczMTA1NzY4MCwiZXhwIjoxNzY3MjI1NTk5fQ.eyJpZCI6ImUxYWQ2ZjBiLTYyNDAtNGU4OS1hM2RiLTI3MzUzNWE1N2NhYSIsImRhdGEiOnt9LCJyYW5kb20iOiJjYThkODA5OWYyOTVlMDE2OWRiYzNmNTFhZjZmZTJlMyJ9.j2pNeaZVz9E_4).

ETHICS STATEMENT

All patient samples were collected in accordance with the Declaration of Helsinki and after approval by the appropriate Institutional Review Board (RAS ID: 199833; REC reference: 16/LO/1376; Dan Royston). Written informed consent was obtained from all participants prior to sample collection.

FUNDING

R.K.S. is an Oncode Investigator and is supported by ERC grants (Rewind-MF ERC-CoG 101124542; deFIBER ERC-StG 757339 and PoC DeAlarmin) and a ZonMW VIDI grant. This work was in part supported by grants of the Deutsche Forschungsgemeinschaft (DFG) (German Research Foundation) to H.F.E.G. (417911533), R.K. (KR 4073/9-1), R.K.S. (504777725, 417911533, and 514007497), and I.G.C. (417911533). The project received funding from the program "Netzwerke 2021," an initiative of the Ministry of Culture and Science of the State of North

Rhine-Westphalia (CANTAR network). R.K., I.G.C., and R.K.S. are members of the E:MED Consortia Fibromap and the consortium CureFib funded by the German Ministry of Education and Science (BMBF). H.F.E.G. is supported by a Gilead Research Scholar Award in Oncology/Hematology, a ZonMW VENI grant, a KWF (Dutch Cancer Society) Exploration grant and an Erasmus Medical Center Fellowship. Open Access funding enabled and organized by Projekt DEAL.

SUPPORTING INFORMATION

Additional supporting information can be found in the online version of this article.

ORCID

Daniel Royston https://orcid.org/0000-0002-5151-2378
Hélène F. E. Gleitz https://orcid.org/0000-0001-6138-8916
Rafael Kramann https://orcid.org/0000-0003-4048-6351
César Nombela-Arrieta https://orcid.org/0000-0003-0415-259X
Rebekka K. Schneider https://orcid.org/0000-0002-0749-1565

REFERENCES

1. Friedman SL, Sheppard D, Duffield JS, Violette S. Therapy for fibrotic diseases: nearing the starting line. *Sci Transl Med*. 2013;5(167):167sr1.
2. Henderson NC, Rieder F, Wynn TA. Fibrosis: from mechanisms to medicines. *Nature*. 2020;587(7835):555-566.
3. Kuppe C, Ibrahim MM, Kranz J, et al. Decoding myofibroblast origins in human kidney fibrosis. *Nature*. 2021;589(7841):281-286.
4. Kramann R, Schneider RK, DiRocco DP, et al. Perivascular Gli1+ progenitors are key contributors to injury-induced organ fibrosis. *Cell Stem Cell*. 2015;16(1):51-66.
5. Schneider RK, Mullally A, Dugourd A, et al. Gli1$^+$ mesenchymal stromal cells are a key driver of bone marrow fibrosis and an important cellular therapeutic target. *Cell Stem Cell*. 2017;20(6):785-800.e8.
6. Gleitz HFE, Dugourd AJF, Leimkühler NB, et al. Increased CXCL4 expression in hematopoietic cells links inflammation and progression of bone marrow fibrosis in MPN. *Blood*. 2020;136(18):2051-2064.
7. Mendez Luque LF, Blackmon AL, Ramanathan G, Fleischman AG. Key role of inflammation in myeloproliferative neoplasms: instigator of disease initiation, progression. and symptoms. *Curr Hematol Malig Rep*. 2019;14(3):145-153.
8. Leimkühler NB, Gleitz HFE, Ronghui L, et al. Heterogeneous bone-marrow stromal progenitors drive myelofibrosis via a druggable alarmin axis. *Cell Stem Cell*. 2021;28(4):637-652.e8.
9. Méndez-Ferrer S, Bonnet D, Steensma DP, et al. Bone marrow niches in haematological malignancies. *Nat Rev Cancer*. 2020;20(5):285-298.
10. Xiao Y, McGuinness CS, Doherty-Boyd WS, Salmeron-Sanchez M, Donnelly H, Dalby MJ. Current insights into the bone marrow niche: from biology in vivo to bioengineering ex vivo. *Biomaterials*. 2022;286:121568.
11. Schneider RK, Mullally A, Dugourd A, et al. Gli1$^+$ mesenchymal stromal cells are a key driver of bone marrow fibrosis and an important cellular therapeutic target. *Cell Stem Cell*. 2018;23(2):308-309.
12. Shi Y, He G, Lee WC, McKenzie JA, Silva MJ, Long F. Gli1 identifies osteogenic progenitors for bone formation and fracture repair. *Nat Commun*. 2017;8(1):2043.
13. Buhl EM, Djudjaj S, Klinkhammer BM, et al. Dysregulated mesenchymal PDGFR-β drives kidney fibrosis. *EMBO Mol Med*. 2020;12(3):e11021.
14. Worthley DL, Churchill M, Compton JT, et al. Gremlin 1 identifies a skeletal stem cell with bone, cartilage, and reticular stromal potential. *Cell*. 2015;160(1-2):269-284.
15. Sivaraj KK, Majev PG, Jeong HW, et al. Mesenchymal stromal cell-derived septoclasts resorb cartilage during developmental ossification and fracture healing. *Nat Commun*. 2022;13(1):571.
16. Baccin C, Al-Sabah J, Velten L, et al. Combined single-cell and spatial transcriptomics reveal the molecular, cellular and spatial bone marrow niche organization. *Nat Cell Biol*. 2020;22(1):38-48.
17. Chagraoui H, Tulliez M, Smayra T, et al. Stimulation of osteoprotegerin production is responsible for osteosclerosis in mice overexpressing TPO. *Blood*. 2003;101(8):2983-2989.
18. Naba A, Clauser KR, Hoersch S, Liu H, Carr SA, Hynes RO. The matrisome: in silico definition and in vivo characterization by proteomics of normal and tumor extracellular matrices. *Mol Cell Proteomics*. 2012;11(4):M111.014647.
19. Peisker F, Halder M, Nagai J, et al. Mapping the cardiac vascular niche in heart failure. *Nat Commun*. 2022;13(1):3027.
20. Li R, Banjanin B, Schneider RK, Costa IG. Detection of cell markers from single cell RNA-seq with sc2marker. *BMC Bioinformatics*. 2022;23(1):276.
21. Ma X, Robin C, Ottersbach K, Dzierzak E. The Ly-6A (Sca-1) GFP transgene is expressed in all adult mouse hematopoietic stem cells. *Stem Cells*. 2002;20(6):514-521.
22. Martineau C, Najyb O, Signor C, Rassart É, Moreau R. Apolipoprotein D deficiency is associated to high bone turnover, low bone mass and impaired osteoblastic function in aged female mice. *Metabolism*. 2016;65(9):1247-1258.
23. Naba A, Clauser KR, Ding H, Whittaker CA, Carr SA, Hynes RO. The extracellular matrix: tools and insights for the "omics" era. *Matrix Biol*. 2016;49:10-24.
24. Chen Q, Liu Y, Jeong HW, et al. Apelin endothelial niche cells control hematopoiesis and mediate vascular regeneration after myeloablative injury. *Cell Stem Cell*. 2019;25(6):768-783.e6.
25. Sivaraj KK, Jeong HW, Dharmalingam B, et al. Regional specialization and fate specification of bone stromal cells in skeletal development. *Cell Rep*. 2021;36(2):109352.
26. Tratwal J, Bekri D, Boussema C, et al. MarrowQuant across aging and aplasia: a digital pathology workflow for quantification of bone marrow compartments in histological sections. *Front Endocrinol*. 2020;11:480.
27. Coates BA, McKenzie JA, Buettmann EG, et al. Transcriptional profiling of intramembranous and endochondral ossification after fracture in mice. *Bone*. 2019;127:577-591.
28. Ryou H, Sirinukunwattana K, Aberdeen A, et al. Continuous Indexing of Fibrosis (CIF): improving the assessment and classification of MPN patients. *Leukemia*. 2022;37(2):348-358.
29. Gu YC, Nilsson K, Eng H, Ekblom M. Association of extracellular matrix proteins fibulin-1 and fibulin-2 with fibronectin in bone marrow stroma. *Br J Haematol*. 2000;109(2):305-313.
30. Nagai JS, Leimkühler NB, Schaub MT, Schneider RK, Costa IG. CrossTalkeR: analysis and visualization of ligand–receptor networks. *Bioinformatics*. 2021;37(22):4263-4265.
31. Matsushita Y, Nagata M, Kozloff KM, et al. A Wnt-mediated transformation of the bone marrow stromal cell identity orchestrates skeletal regeneration. *Nat Commun*. 2020;11(1):332.
32. Lam AP, Gottardi CJ. β-Catenin signaling: a novel mediator of fibrosis and potential therapeutic target. *Curr Opin Rheumatol*. 2011;23(6):562-567.
33. Stoddart A, Wang J, Hu C, et al. Inhibition of WNT signaling in the bone marrow niche prevents the development of MDS in the Apc-del/+ MDS mouse model. *Blood*. 2017;129(22):2959-2970.
34. Ramachandran P, Dobie R, Wilson-Kanamori JR, et al. Resolving the fibrotic niche of human liver cirrhosis at single-cell level. *Nature*. 2019;575(7783):512-518.
35. Sarkaria SM, Zhou J, Bao S, et al. Systematic dissection of coordinated stromal remodeling identifies Sox10 glial cells as a therapeutic target in myelofibrosis. *Cell Stem Cell*. 2023;30(6):832-850.e6.

36. Decker M, Martinez-Morentin L, Wang G, et al. Leptin-receptor-expressing bone marrow stromal cells are myofibroblasts in primary myelofibrosis. *Nat Cell Biol*. 2017;19(6):677-688.
37. Acar M, Kocherlakota KS, Murphy MM, et al. Deep imaging of bone marrow shows non-dividing stem cells are mainly perisinusoidal. *Nature*. 2015;526(7571):126-130.
38. Hooper AT, Butler JM, Nolan DJ, et al. Engraftment and reconstitution of hematopoiesis is dependent on VEGFR2-mediated regeneration of sinusoidal endothelial cells. *Cell Stem Cell*. 2009;4(3):263-274.
39. Ganesan S, Awan-Toor S, Guidez F, et al. Comprehensive analysis of mesenchymal cells reveals a dysregulated TGF-β/Wnt/HOXB7 axis in patients with myelofibrosis. *JCI Insight*. 2024;9(23):e173665. doi:10.1172/jci.insight.173665
40. Gu W, Tong J, Fu R, et al. Molecular analysis of phenotypic heterogeneity in JAK2V617F-positive myeloproliferative neoplasms reveals a potential target for therapy. *Br J Haematol*. 2023;201(4):690-703.
41. Gomariz A, Helbling PM, Isringhausen S, et al. Quantitative spatial analysis of haematopoiesis-regulating stromal cells in the bone marrow microenvironment by 3D microscopy. *Nat Commun*. 2018;9(1):2532.
42. Hao Y, Hao S, Andersen-Nissen E, et al. Integrated analysis of multimodal single-cell data. *Cell*. 2021;184(13):3573-3587.e29.